

Melting performance enhancement in a thermal energy storage unit using active vortex generation by electric field

Selvakumar, R. Deepak; Wu, Jian; Afgan, Imran; Ding, Yulong; Alkaabi, Ahmed K.

DOI:

[10.1016/j.est.2023.107593](https://doi.org/10.1016/j.est.2023.107593)

License:

Creative Commons: Attribution (CC BY)

Document Version

Publisher's PDF, also known as Version of record

Citation for published version (Harvard):

Selvakumar, RD, Wu, J, Afgan, I, Ding, Y & Alkaabi, AK 2023, 'Melting performance enhancement in a thermal energy storage unit using active vortex generation by electric field', *Journal of Energy Storage*, vol. 67, 107593. <https://doi.org/10.1016/j.est.2023.107593>

[Link to publication on Research at Birmingham portal](#)

General rights

Unless a licence is specified above, all rights (including copyright and moral rights) in this document are retained by the authors and/or the copyright holders. The express permission of the copyright holder must be obtained for any use of this material other than for purposes permitted by law.

- Users may freely distribute the URL that is used to identify this publication.
- Users may download and/or print one copy of the publication from the University of Birmingham research portal for the purpose of private study or non-commercial research.
- User may use extracts from the document in line with the concept of 'fair dealing' under the Copyright, Designs and Patents Act 1988 (?)
- Users may not further distribute the material nor use it for the purposes of commercial gain.

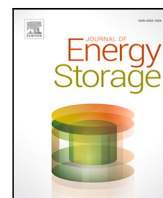
Where a licence is displayed above, please note the terms and conditions of the licence govern your use of this document.

When citing, please reference the published version.

Take down policy

While the University of Birmingham exercises care and attention in making items available there are rare occasions when an item has been uploaded in error or has been deemed to be commercially or otherwise sensitive.

If you believe that this is the case for this document, please contact UBIRA@lists.bham.ac.uk providing details and we will remove access to the work immediately and investigate.



Research Papers

Melting performance enhancement in a thermal energy storage unit using active vortex generation by electric field

R. Deepak Selvakumar^a, Jian Wu^b, Imran Afgan^{c,d}, Yulong Ding^e, Ahmed K. Alkaabi^{a,*}

^a Department of Nuclear Engineering and Emirates Nuclear Technology Center (ENTC), Khalifa University of Science and Technology, Abu Dhabi, United Arab Emirates

^b Heilongjiang Key Laboratory of Micro- and Nano-scale Fluid Flow and Heat Transfer and School of Energy Science and Engineering, Harbin Institute of Technology, Harbin 150001, PR China

^c Department of Mechanical Engineering and Emirates Nuclear Technology Center (ENTC), Khalifa University of Science and Technology, Abu Dhabi, United Arab Emirates

^d Department of MACE, University of Manchester, Manchester M13 9PL, United Kingdom

^e Birmingham Center for Energy Storage and School of Chemical Engineering, University of Birmingham, Birmingham B15 2TT, United Kingdom

ARTICLE INFO

Keywords:

Energy storage

Melting

Electrohydrodynamics

Charge injection

Active method

ABSTRACT

Latent heat thermal energy storage (LHTES) devices aid in efficient utilization of alternate energy systems and improve their ability to handle supply–demand fluctuations. A numerical analysis of melting performance in a shell-and-tube LHTES unit in the presence of a direct current (DC) electric field has been performed. The governing equations of fluid flow, heat transfer, electric potential and charge conservation are solved using a customized finite-volume solver built in the open-source framework of OpenFOAM. Enthalpy-porosity method based fixed grid approach is used to track the melt interface. Primary objective of the study is to highlight the interface and flow morphology evolution in the presence of electric field induced flow and to evaluate the melting performance of the LHTES unit. The transient evolution of the melting process in the presence of electric field has been mapped in terms of total liquid fraction, kinetic energy density and mean Nusselt number. The charge injection from the tube surface generates multiple electrohydrodynamic (EHD) flow vortices in the liquid region. Thus, the inherent uni-cellular flow structure of the natural convection driven melting is disrupted. The multi-cellular flow structure with stronger velocity distribution enhances mixing and heat transfer. Melting performance at various levels of applied voltages ($0 \leq V \leq 10$ kV) in both vertical and horizontal orientations of the LHTES unit has been quantified in terms of charging time and total power storage. The charging time gets shorter and total power storage gets higher with increasing applied voltages. In the vertical orientation, a maximum 82.52% reduction in charging time and 80.85% increase in net power storage is achieved. In the horizontal orientation, weaker buoyancy force leads to stronger influence of the electric field. A maximum of 89.61% reduction in charging time and 88.35% increase in power storage is achieved in the horizontal orientation. The results of this study aid in understanding the mechanism of EHD flow assisted melting and provide a reference for design of a shell-and-tube LHTES unit with improved performance.

1. Introduction

Increasing global energy consumption and the global warming have pushed the researchers to shift towards greener and sustainable energy resources with lesser carbon footprint. Solar/wind energy are considered a potential substitute for conventional fossil fuel based energy production. However, the availability of the solar and wind energy is discontinuous with respect to time [1]. Nuclear energy is also an alternate energy source with lesser carbon footprint [2]. But, nuclear power plants are efficient only when operated at full load with constant output and thus, have a limited load-following capability

with the respect to the supply grid requirements [3]. In an attempt to overcome these limitations, latent heat thermal energy storage (LHTES) has become a critical component in energy production systems with intermittent availability or poor load-following capability [4]. LHTES systems coupled with power production plants store the excess energy when it is available in excess and release when the source is not available or the demand in the supply grid is high [5–8]. LHTES systems are popular owing to their simple design, high volumetric efficiency, high energy storage density and minimum energy loss [9].

* Corresponding author.

E-mail address: ahmed.alkaabi@ku.ac.ae (A.K. Alkaabi).

<https://doi.org/10.1016/j.est.2023.107593>

Received 21 February 2023; Received in revised form 10 April 2023; Accepted 29 April 2023

Available online 11 May 2023

2352-152X/© 2023 The Author(s). Published by Elsevier Ltd. This is an open access article under the CC BY license (<http://creativecommons.org/licenses/by/4.0/>).

Nomenclature**Notations**

\vec{E}	Electric field [Vm^{-1}].
\vec{J}	Current density [Am^{-2}].
\vec{u}	Velocity vector [ms^{-1}].
C	Charge injection parameter.
C_p	Specific heat capacity [$\text{Jkg}^{-1}\text{K}^{-1}$].
D	Ionic diffusivity [m^2s^{-1}].
D_S	Diameter of the shell [mm].
D_T	Diameter of the tube [mm].
f	Local liquid fraction.
H	Height of the LHTES unit [m].
K	Ionic mobility [$\text{m}^2\text{V}^{-1}\text{s}^{-1}$].
k	Thermal conductivity [$\text{Wm}^{-1}\text{K}^{-1}$].
KE	Kinetic energy density [Jm^{-3}].
L	Latent heat of fusion [kJkg^{-1}].
P	Power [Js^{-1}].
p	Pressure [$\text{kgm}^{-1}\text{s}^{-2}$].
q	Charge density [Cm^{-3}].
T	Electric Rayleigh number.
t	Time [s].
V	Electric potential [V].
v	Volume [m^3].
\vec{g}	Gravitational acceleration [ms^{-2}].

Greek Symbols

α	Thermal diffusivity [m^2s^{-1}].
β	Thermal expansion coefficient [K^{-1}].
μ	Dynamic viscosity [$\text{kgm}^{-1}\text{s}^{-1}$].
ν	Kinematic viscosity [m^2s^{-1}].
ρ	Density [kgm^{-3}].
σ	Electric conductivity [Sm^{-1}].
θ	Temperature [K].
ϵ	Dielectric permittivity [Fm^{-1}].

Superscripts/Subscripts

0	Initial value.
∞	Ambient value.
s, l	Solid, liquid phase.

However, the thermal conductivity of phase change materials (PCMs) is inherently low leading to slow melting process and energy storage rates [10]. Researchers have attempted to use several techniques to enhance the melting process in the LHTES units.

Performance improvement in LHTES units can be classified into three categories, namely (i) extending the heat transfer area, (ii) improving the effective thermal conductivity of the PCM and (iii) intensifying the heat transfer rate by inducing flow motion in the melt region. Inclusion of pins, fins and micro-encapsulation of the PCMs are the common approaches used to increase the heat transfer area [11]. Several studies have been reported on the investigation of effects of fin dimensions [12], fin orientation [13] and fin numbers [14] on the melting rate enhancement. Although, the fins increase the heat transfer surface area, over utilization of fins damps the natural convective flow. Recently, researchers have attempted to use complex fractal shaped fins for melting enhancement in LHTES units [15,16]. However, manufacturing of LHTES units with complex fin shapes is difficult [17,18]. Micro-encapsulation of PCM also increases the heat

transfer area, where each individual micro-capsule acts as a separate LHTES unit with higher surface area to volume ratio [19]. But, micro-encapsulation of PCM is a time consuming, labor intensive process and are less scalable to large capacity LHTES systems [20]. Researcher are working towards microfluidic method based encapsulation of PCMs to overcome these limitations [21]. Addition of fine nanoparticles with high thermal conductivity metallic nanoparticles increase the effective thermal conductivity of the PCM and enables faster melting rates [22,23]. In addition metallic nanoparticles act as nucleation sites for melting [24]. Adding non-metallic nanoparticles improve the thermal stability and increase the energy storage density. However, deposition and coagulation of nanoparticles is a big concern [25,26]. Likewise, researchers have attempted to incorporate metallic foams into the PCMs to improve the effective thermal conductivity. Metallic foams enhance the thermal conductivity and also, improve the thermal stability of the LHTES system. However, embedding metallic foams into PCMs increase complexity in construction and maintenance of LHTES systems and also, significantly increase the net weight [27]. Metallic foams are also susceptible for corrosion and can deteriorate over time, reducing the effectiveness and lifespan of the LHTES units [28].

Melting enhancement techniques discussed above are passive methods that does not involve any secondary fluid flow. Active techniques of melting enhancement involve additional fluid flow induced by a secondary mechanism. LHTES units subjected to mechanical and acoustic vibrations actively increase the velocity distribution and mixing in the liquid region and enhance the melting process [29,30]. However, incorporating these acoustic and mechanical vibrations devices increased the system complexity, affected the mechanical stability and notably increased the total power consumption [30]. Few researchers have attempted to employ magnetic field induced fluid motion to improve the melting process. However, the action of magnetic field deteriorated the melting rate [31,32]. Review of the available literature reveals that the works on performance improvement in LHTES units using active methods are very scarce in literature. Majority of the studies on performance improvement in LHTES units are concerned with passive techniques like using fins, metal foams, micro-encapsulation and nano-additives. Very few studies have explored the possibility of using active techniques based on magnetic field induced flows, acoustic and mechanical vibrations, etc. Employment of electric field induced EHD flow based active method to enhance the heat transfer in solid-liquid phase change process is relatively a very new research direction, getting explored only in the past few years.

For the first time in literature, Nakhla et al. [33–36] performed a series of experiments on melting in the presence of electric field. All their experiments reported a notable decrease in charging time with the application of electric field. They reported extraction of semi-solid PCM material from the mushy interface region into the bulk liquid region and termed it as “solid extraction” similar to the liquid extraction observed in boiling process exposed to an electric field [37]. Based on the subsequent observations of their studies, they inferred that the charge injection mechanism leading to electroconvection flow cells primarily contributed to the enhancement in melting. Experiments of EHD assisted melting performed by Nakhla et al. [33–36] had complex setups with an array of wire electrodes which limited the ability to isolate and study the underlying mechanism in EHD assisted melting. To overcome this limitation, Sun et al. [38–41] performed a series of EHD melting experiments in simple configurations to provide deeper insights on the underlying mechanism of EHD assisted melting. In all their experiments, they identified the Coulomb force to be responsible for the melting enhancement. In addition, their studies provided deeper insights on the charge generation mechanisms. The strength of electric field determines the charge generation mechanism. Under weak electric field, the free charges are produced by the conduction mechanism. Whereas, charge injection took place when the electric field is strong. Results of Sun et al. [38–41] reported that the strength of electric field, charge generation mechanism, polarity of the applied voltage and the

resultant direction of fluid flow are all important parameters that determine the melting performance. A recent experimental study on EHD assisted melting of paraffin wax by Hassan and Cotton [42] reported an melting enhancement of 4.75 times by the application of electric field. It was reported that the Coulomb force is primarily responsible for the solid extraction phenomenon and melting enhancement.

Following the experimental studies on EHD assisted melting, numerical models for EHD assisted melting were reported in literature. Luo et al. [43] developed a lattice Boltzmann method (LBM) based model for EHD assisted melting and analyzed the roles of electric Rayleigh number (T), Prandtl number (Pr) and Stefan number (St) on melting enhancement. It was reported that the higher values of T and lower values of St favored maximum melting enhancement due to the action of Coulomb force. Using the LBM model for melting developed by Luo et al. [43], Lu et al. [44] performed a heat transfer analysis of EHD solid-liquid phase change. A maximum 60% enhancement in melting speed was reported and the melting process became independent of the Rayleigh number (Ra) at high values of electric Rayleigh number (T). A finite-volume method (FVM) based numerical algorithm for EHD assisted melting was developed by selvakumar et al. [45]. Multiple stages in the EHD assisted melting process were identified and the mechanism of EHD assisted melting was highlighted. Lower values of Ra and higher values of T favored maximum melting enhancement by Coulomb force. Subsequently, a numerical study considering the combined action of buoyancy, Coulomb and dielectric forces was performed by Selvakumar et al. [46]. It was confirmed that the Coulomb force is the main reason for melting enhancement and dielectric force plays a minor role only in the earlier stages of EHD melting. At higher values of T , the melting process was purely driven by the electroconvective flow. Recently, Endigeri et al. [47] performed a numerical analysis of EHD assisted melting in a square cavity with a circular wire electrode. Although, larger wire electrode produced stronger EHD flow, the resultant EHD flow is damped by the presence of large electrode. Thus, small wire electrode produced higher melting enhancement, as compared to larger wire electrode.

Above literature review indicates that the research on performance improvement of LHTES units are mainly concentrated on the employment of passive methods [11]. Very few studies deal with active methods for melting enhancement. EHD flow assisted melting process is a relatively new research direction. Results available in literature indicate that organic PCMs are electrically insulating materials with good dielectric strength to withstand strong electric fields. Due to the low electrical conductivity, the energy consumption is very small even at very high applied voltages. Furthermore, EHD based systems have simple design, quick response and vibration free operation [48]. Thus, electric field-based control of melting is a viable and economic technique that deserves more attention. Likewise, the effect of electric field on melting is very less explored and most of these studies are limited to basic analysis to understand the mechanism of EHD assisted melting. To the best of our knowledge, no work has been reported in the archived literature to investigate the effect of electric field on the melting performance in a shell-and-tube LHTES unit. In an attempt to bridge this gap and to provide more insights, this study presents a numerical investigation of melting performance in a shell-and-tube LHTES unit in the presence of an EHD flow induced by charge injection. The flow features, heat transfer characteristics and melt interface morphology in the presence of electric field in a shell-and-tube LHTES unit are presented. The shift in the uni-cellular flow morphology of the natural convection melting to multi-cellular flow structure in EHD assisted melting process is highlighted. Furthermore, effects of electric field induced flow on melting performance in both vertical and horizontal orientations of the shell-and-tube LHTES unit are studied. The melting performance is quantified in terms of charging time and power storage.

Table 1

Properties of PCM (Paraffin wax) [35,38,49,53].

Property	Value
Liquid Density [ρ_l]	760.00 kgm ⁻³
Solid Density [ρ_s]	870.00 kgm ⁻³
Liquid Specific Heat Capacity [$C_{p,l}$]	2400.00 Jkg ⁻¹ K ⁻¹
Solid Specific Heat Capacity [$C_{p,s}$]	1800.00 Jkg ⁻¹ K ⁻¹
Liquid Thermal Conductivity [k_l]	0.15 Wm ⁻¹ K ⁻¹
Solid Thermal Conductivity [k_s]	0.24 Wm ⁻¹ K ⁻¹
Dynamic Viscosity [μ_l]	3.42×10^{-3} kgm ⁻¹ s ⁻¹
Thermal Expansion Coefficient [β]	1×10^{-6} K ⁻¹
Latent Heat of Fusion [L]	192.00 kJkg ⁻¹
Solidus Temperature [θ_{sol}]	331.00 K
Liquidus Temperature [θ_{liq}]	333.00 K
Liquid Dielectric Permittivity [ϵ_l]	1.771×10^{-11} Fm ⁻¹
Solid Dielectric Permittivity [ϵ_s]	1.992×10^{-11} Fm ⁻¹
Liquid Ionic Mobility [K_l]	7.50×10^{-8} m ² s ⁻¹ V ⁻¹
Solid Ionic Mobility [K_s]	7.50×10^{-7} kgm ⁻³

2. Problem formulation

2.1. Physical description of the problem and computational domain

A shell-and-tube latent heat thermal energy storage (LHTES) device of height $H = 1$ m under the influence of electrohydrodynamic flow induced by charge injection is considered. The diameters of the shell and tube are $D_s = 36$ mm and $D_T = 12$ mm, respectively. The dimensions and operating temperature of the LHTES module are adopted from the experimental study of Kibria et al. [49]. Present study considers 2D slices of the shell-and-tube LHTES unit in vertical (case 1) and horizontal (case 2) orientations [50,51]. A schematic diagram of the TES unit, computational domain in vertical and horizontal orientations along with the associated boundary conditions are presented in Fig. 1. The shell of the LHTES unit is initially filled with solid PCM (paraffin wax) at ambient temperature ($\theta_\infty = 298.15$ K). Heat transfer fluid (HTF) at 361.15 K is considered to flow through the tube. The flow rate is sufficiently high such that the difference between the inlet and outlet temperature is less than 0.5 K [49]. Thus, a constant temperature ($\theta_H = 361.15$ K) boundary condition is considered at the tube wall (flow of HTF is not considered). No-slip boundary condition is considered at the wall surfaces. The top, bottom and shell walls are set to be adiabatic. The tube wall is connected to a high voltage power supply (V_0), whereas, the shell wall is grounded. The top and bottom walls are electrically insulated. Thus, the charge injection takes place from the tube wall (emitter electrode) towards the shell wall (collector electrode). A constant, homogeneous and autonomous charge injection is considered at the emitter electrode [43,52]. Accurate experimental measurement of charge density is not possible. To overcome this limitation, a non-dimensional charge injection parameter $C = \frac{q_0(D_s - D_T)}{2\epsilon_l V_0}$ is commonly used in the literature. Here, q_0 is the charge density at the electrode surface and ϵ_l is the dielectric permittivity. The injection parameter is generally varied in three levels 0.1, 1 and 10, corresponding to weak, medium and strong charge injection regimes, respectively. In the present study, medium charge injection with $C = 1$ is considered [52]. The thermo-physical and dielectric properties of the PCM are listed in Table 1. It is necessary to mention that the ionic mobility of the PCM in liquid state is calculated by Walden's rule [53] and the ionic mobility in solid state is one order of magnitude higher than that in liquid state [34].

2.2. Governing equations

The two-way coupled governing equations for fluid flow, heat transfer, solid-liquid phase change, electric potential and charge transport are considered based on the following assumptions [46,54]:

- The flow is two-dimensional, incompressible and Newtonian.

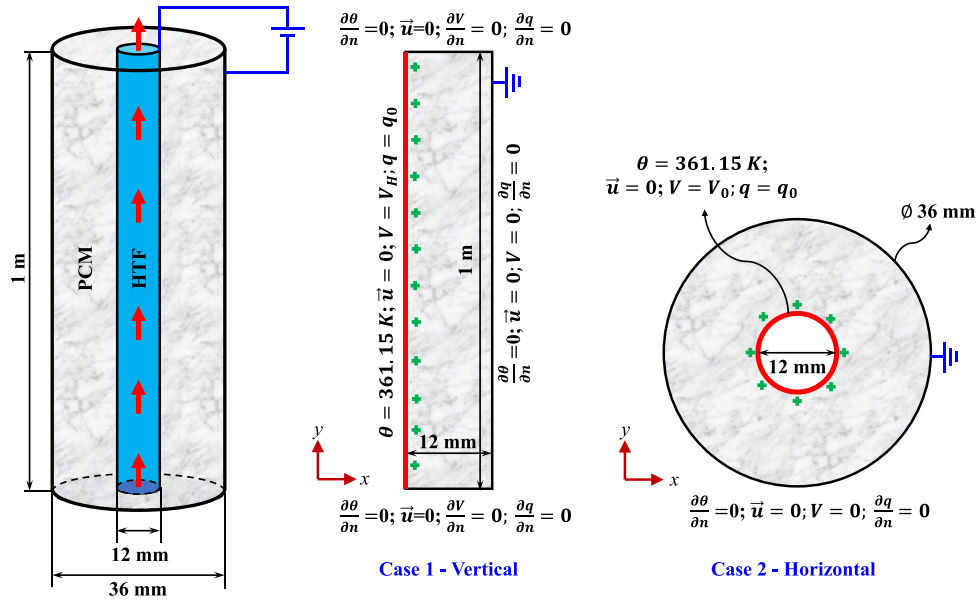


Fig. 1. A schematic representation of the latent heat thermal energy storage (LHTES) unit and the computational domains for case 1 (Vertical orientation) and case 2 (Horizontal orientation) with the associated boundary conditions (The images are not to scale).

- The PCM is a dielectric material and the electric current is negligible. Thus, magnetic effects, joule heating and the heating from the electrode surface are negligible.
- Thermo-physical properties and dielectric properties are different for solid and liquid phases but are constant with respect to temperature in each individual phase.
- The density variation in the liquid region is calculated by Boussinesq approximation.
- The solid phase is rigidly fixed to the wall.

Continuity equation:

$$\nabla \cdot \vec{u} = 0, \quad (1)$$

Momentum equation:

$$\frac{\partial \vec{u}}{\partial t} + \nabla \cdot (\vec{u}\vec{u}) = -\nabla p + \nu_l \nabla^2 \vec{u} - \vec{g} [1 - \beta (\theta - \theta_\infty)] + q\vec{E} + \frac{1}{2} \vec{E}^2 \nabla \epsilon + S_u \quad (2)$$

Energy equation:

$$\frac{\partial \theta}{\partial t} + \nabla \cdot (\vec{u}\theta) = \nabla \cdot (\alpha_{l/s} \nabla \theta) + S_\theta \quad (3)$$

Poisson equation for electric potential:

$$\nabla \cdot (\epsilon_{l/s} \nabla V) = -q_{l/s} \quad (4)$$

Electric field:

$$\vec{E}_{l/s} = -\nabla V \quad (5)$$

Charge transport equation:

$$\frac{\partial q_{l/s}}{\partial t} + \nabla \cdot \vec{J} = 0; \quad \vec{J} = (K_{l/s} E_{l/s} + \vec{u})q_{l/s} - D_{l/s} \nabla q_{l/s} \quad (6)$$

Here, $\vec{u} = [u_x, u_y]$ and $\vec{E} = [E_x, E_y]$ denote the velocity and electric field vectors, respectively. $\vec{g} [1 - \beta (\theta - \theta_\infty)]$ is the buoyancy body force term (Boussinesq approximation). β is the volumetric thermal expansion coefficient. $\vec{g} = g \mathbf{e}_y$ ($g > 0$) represent the acceleration due to gravity and $\mathbf{e}_y = [0, 1]$ is the unit normal vector. The terms $q\vec{E}$ and $\frac{1}{2} \vec{E}^2 \nabla \epsilon$ in Eq. (2) represent the Coulomb and dielectric forces, respectively. In Eq. (3), the terms ν , θ and α denote the kinematic viscosity, temperature and thermal diffusivity, respectively. The source term S_θ in Eq. (3) is given as [55]:

$$S_\theta = - \frac{[\nabla \cdot (\vec{u}(Lf)) + \frac{\partial (Lf)}{\partial t}]}{C_p} \quad (7)$$

Here, L is the latent heat of fusion, C_p is the specific heat capacity and f is the local liquid fraction in a control volume. The local liquid fraction f is a function of temperature θ and is expressed as follows:

$$f(\theta) = \begin{cases} 0 & \theta \geq \theta_{liq} \\ \frac{\theta - \theta_{sol}}{\theta_{liq} - \theta_{sol}} & \theta_{liq} > \theta \geq \theta_{sol} \\ 1 & \theta < \theta_{sol} \end{cases} \quad (8)$$

In Eq. (8), θ_{liq} and θ_{sol} denote the liquidus and solidus temperatures of the PCM, respectively. The term $S_u = A\vec{u}$ in Eq. (2) is a source term to switch the velocity to zero in the solid region [55,56]. A is expressed as a linear function of local liquid fraction f as $A = -\zeta(1 - f)$. The constant ζ should take a sufficiently high value such that the term A will override all other terms in the momentum equation, within the solid and mushy region. The source term S_u becomes zero within the liquid domain ($f = 1$). In Eqs. (4) and (6), V , ϵ , \vec{J} , q , K and D represent the electric potential, dielectric permittivity, current density, charge density, ionic mobility and charge diffusivity, respectively. The subscript 'l/s' represents the liquid or solid properties calculated as a function of local liquid fraction.

3. Numerical procedure and validation

The open-source FVM-based framework of OpenFOAM® is used to solve the governing equations. The standard finite-volume procedures available in OpenFOAM® are used to discretize the governing equations. The Laplacian and gradient terms are discretized using the central differencing and cubic schemes, respectively. The Quadratic Upwind Interpolation for Convective Kinetics (QUICK) scheme is used to discretize the convective terms in the momentum and energy equations. The electromigration term in the charge-transport equation (Eq. (6)) are transformed similar to a traditional convective terms as described in Ref. [45]. This transformation of the electromigration term helps in using an implicit discretization. The diffusion term in the charge-transport equation is negligible. Thus, the charge-transport equation is a hyperbolic equation with strong convection dominance [53]. This equation suffers from numerical instability similar to high Peclet number convective flows. Thus, the convective terms in the charge-transport equation are discretized using a deferred correction approach based on the total variation diminishing (TVD) VanLeer scheme, as demonstrated in Ref. [53]. The local derivative terms in the governing equations are

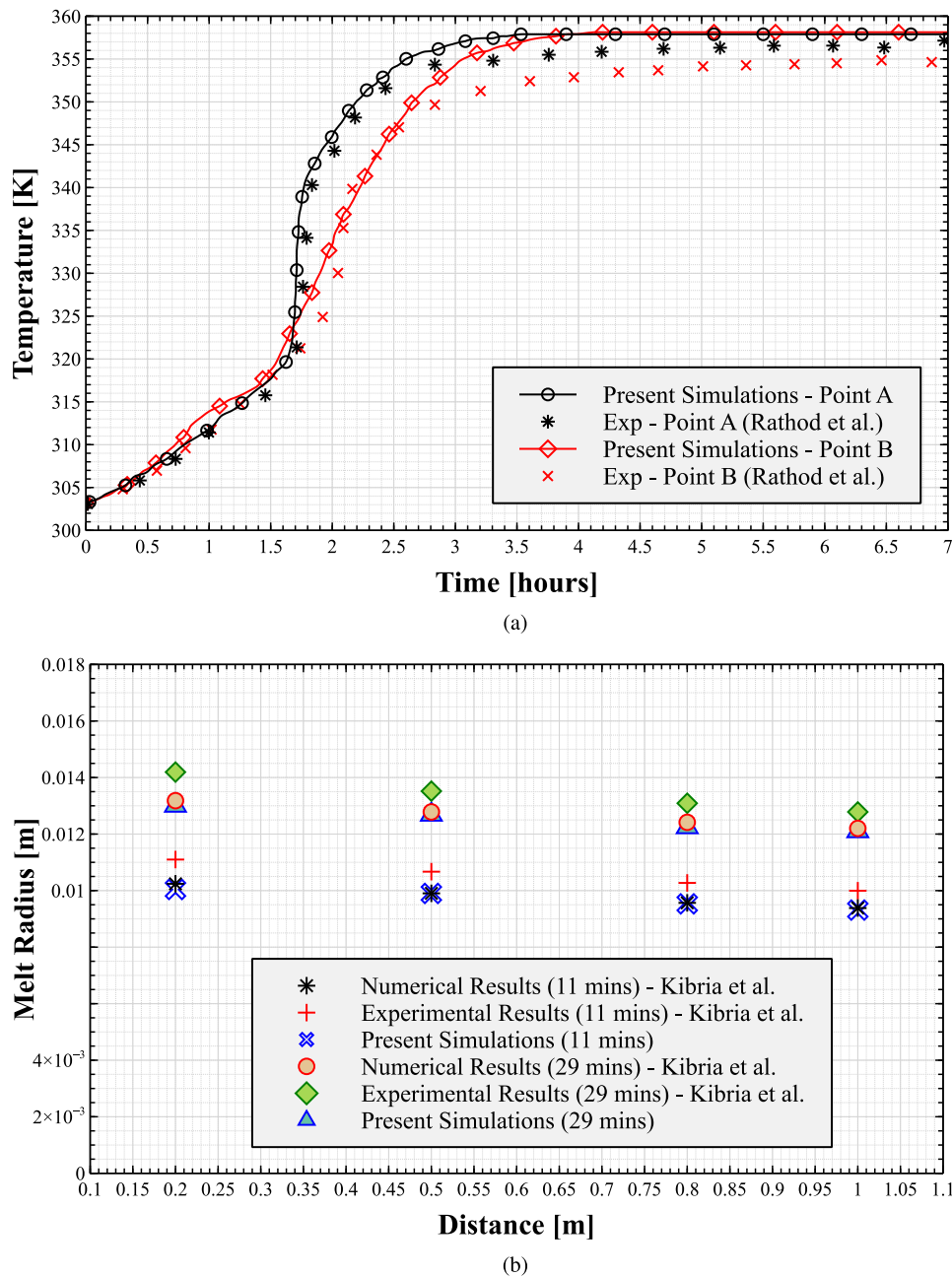


Fig. 2. Comparison of present numerical results with experimental and numerical data for melting in a shell-and-tube LHTES unit from literature. (a) Time variation of temperature at two monitor points (A & B) in a vertical LHTES unit [57] and (b) Melt radius along the length of an horizontal LHTES unit at two instantaneous time moments [49].

discretized using the implicit Euler backward method. The absolute tolerance of all variables is set to 1×10^{-8} . The numerical implementation, discretization, update of source terms, treatment of electromigration term in the charge conservation equation are described elaborately in our previous works [45,46].

A detailed validation of the numerical solver with reference to standard benchmark cases of melting, electric field and charge transport are presented in [45,46]. The problem considered in this study is a combination of melting of a PCM in a shell and tube LHTES unit assisted by the EHD flow in the liquid region. Thus, additional validation cases are presented to establish the capability of the numerical solver to handle the flow and heat transfer physics involved in the problem considered in this study. To begin with, a case of melting (without electric field) in a shell and tube LHTES unit is considered. Rathod et al. [57] performed an experimental study of melting and heat transfer in a vertical shell-and-tube LHTES unit. Experimental results for the time variation of

temperature at two monitor points (A - 0.2 m from the top and B - 0.4 m from the top) in the middle of the distance between the tube and shell were provided in Ref. [57]. A 2D numerical simulation of a vertical slice of the vertical shell-and-tube LHTES unit considered in Ref. [57] was carried out. Fig. 2(a) presents the comparison of the experimental results of Rathod et al. [57] and the present simulations. The root mean square (RMS) value of the temperature difference between the numerical and experimental results at point A is 2.22 K. Whereas, the RMS value of temperature difference between the experimental and numerical results at point B is 3.86 K. This agreement is acceptable and in the range of previous numerical results reported in literature [50]. Likewise, an experimental study of an horizontal shell-and-tube LHTES unit by Kibria et al. [49] is also considered for validation. Kibria et al. [49] reported the experimental measurements of the melt radii at two instantaneous time moments along the horizontal length of the LHTES unit. A 3D numerical simulation of the geometry of the LHTES

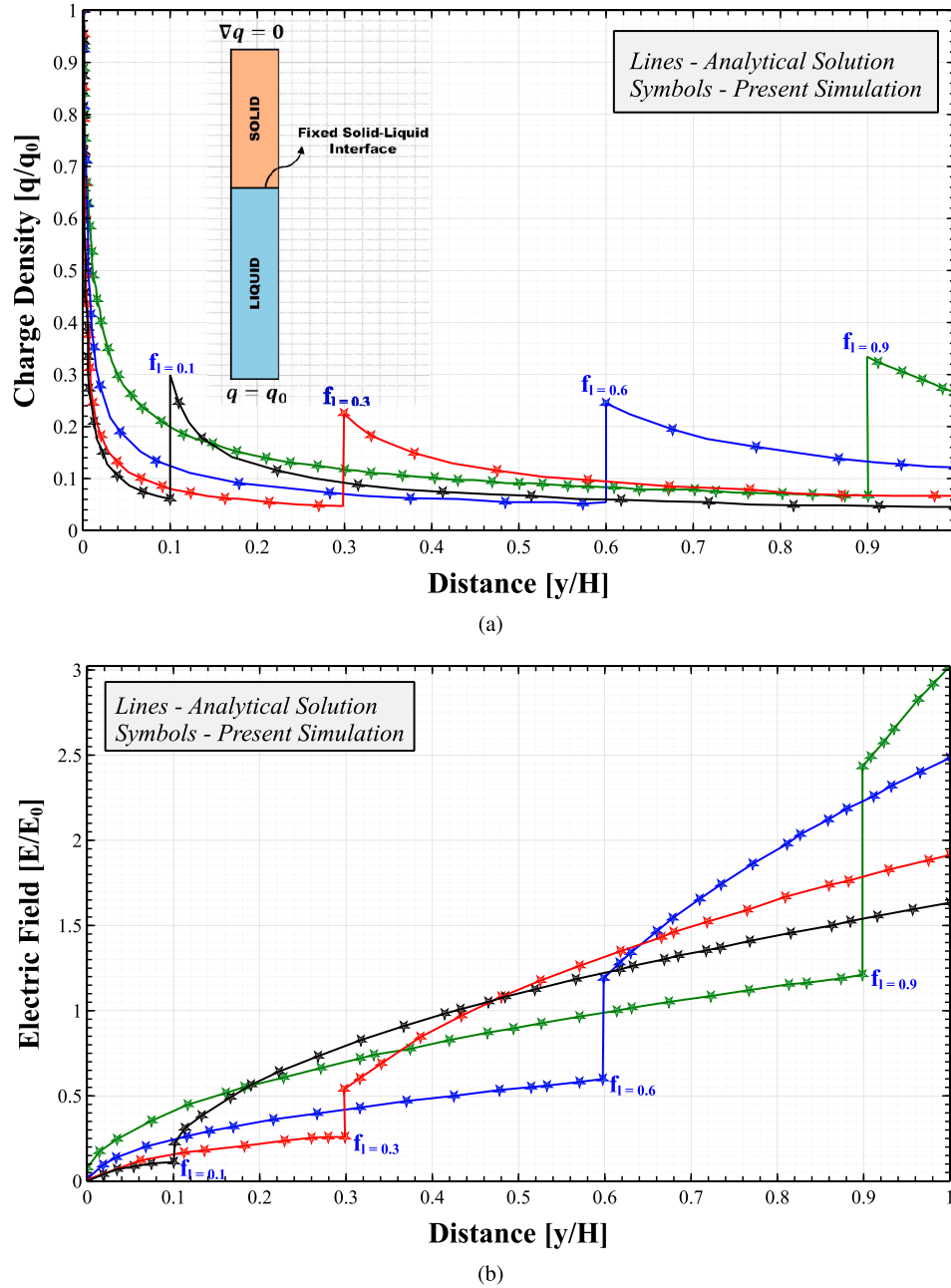


Fig. 3. Comparison of present numerical results for (a) Charge density and (b) Electric field distribution across a solid-liquid interface in a 1-D hydrostatic domain with the analytical results of Luo et al. [43].

unit considered in Ref. [49] was performed. The comparison between the experimental and present numerical predictions of the melt radii along the horizontal length at 11 and 29 mins are reported in Fig. 2(b). The variations between the experimental and present numerical results are within the acceptable limit (maximum deviation less than 3%). The present numerical results and the numerical predictions of Ref. [49] match closely with each other. Secondly, a case of electric field coupled charge transport across a one-dimensional (1D) liquid-solid interface is considered. A vertical 1D domain with different liquid fractions are considered. As the geometry is one-dimensional, the liquid fraction indicates the location of liquid-solid interface along the y -direction. The ionic mobility of the liquid is considered to be 10 times the ionic mobility of the solid ($K_l = 10 \times K_s$). Likewise, the dielectric permittivity of the liquid is 2 times that of the solid ($\epsilon_l = 2 \times \epsilon_s$). The discontinuity in the dielectric properties lead to a sudden step change in charge density and electric field intensity across the interface. Luo et al. [43] provided

analytical solutions for the distribution of the charge density and electric field across an 1D liquid-solid interface. The electric field and charge density distribution across the interface at different locations are presented in Fig. 3. Results obtained by the present numerical solver are in excellent agreement with the analytical solution provided by Luo et al. [43]. The step changes in the charge density and electric field intensity are captured with negligible numerical diffusion and without any nonphysical oscillations. In overall, the capability of the solver to simulate the physics considered in this study is verified.

A 2D rectangular slice for vertical (case 1) and a 2D circular annulus for horizontal (case 2) orientations of the shell-and-tube LHTES unit are considered (refer Fig. 1), herein [50,51]. Thus, a two-dimensional (2D), uniform and structured grid is employed in this study. The grid is chosen based on a grid sensitivity analysis. For both the cases of vertical and horizontal orientations, three different grids G1, G2, and G3 were considered. For case 1 with vertical orientation, G1, G2 and G3 have

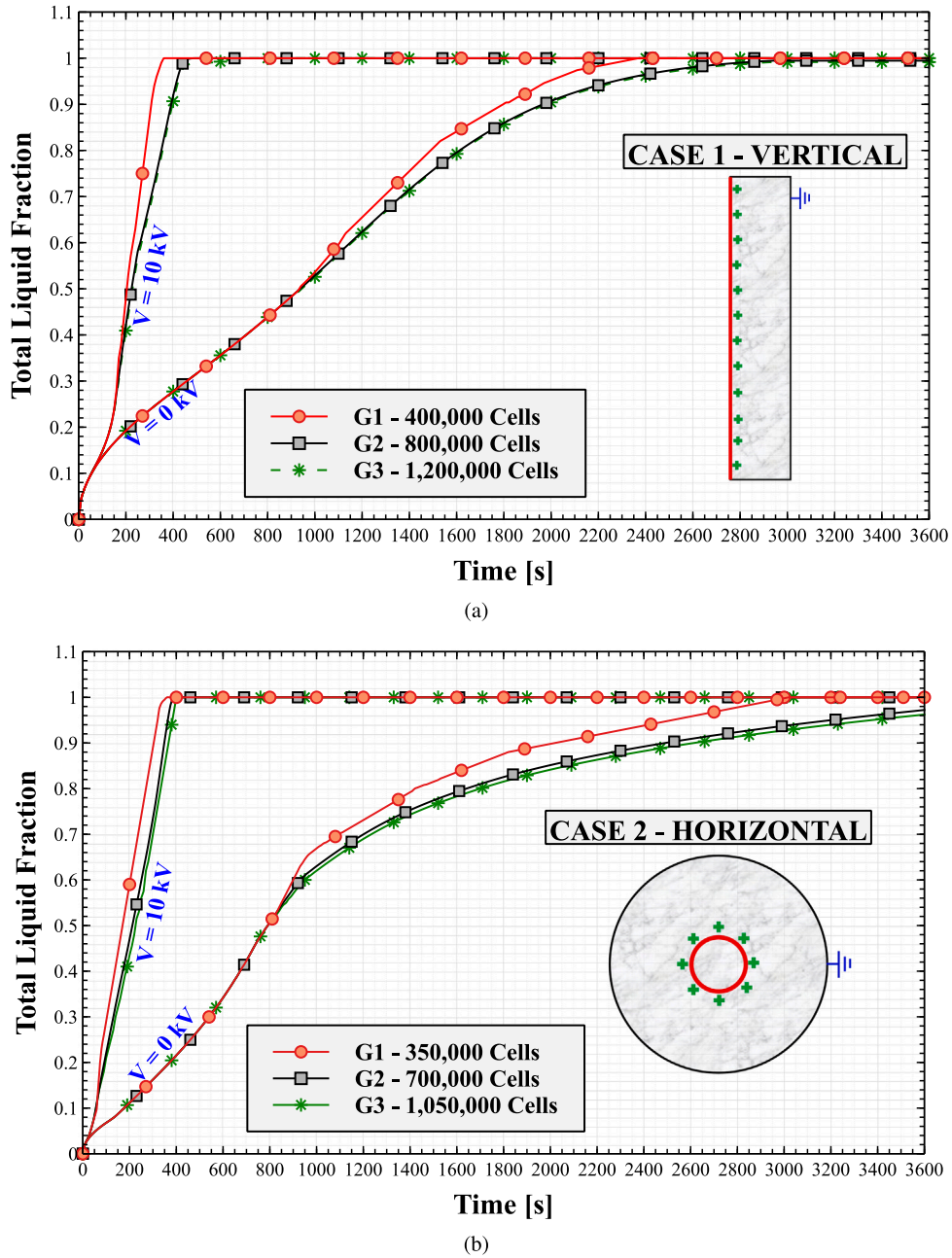


Fig. 4. Time evolution of total liquid fraction in the computation domain for (a) Case 1 : Vertical orientation and (b) Case 2 : Horizontal orientation using three different grids.

400,000, 800,000 and 1,200,000 cells, respectively. Likewise, G1, G2, G3 contain 350,000, 700,000 and 1,050,000 cells, respectively for case 2. Time evolution curves of total liquid fraction in the computational domain is mapped for case 1 and case 2 at $V_0 = 0$ and 10 kV using the three grids in Figs. 4(a) and 4(b), respectively. The variation between the liquid fraction curves using G2 and G3 are negligible for both the cases. The variation between the curves using G1 show notable deviation from those of G2 and G3, for both the cases. Thus, considering both the grid independency of the results and the computational time, grids G2 with 800,000 cells and 700,000 cells are considered for cases 1 and 2, respectively. A sufficiently small time step of 0.001 s has been chosen for all the simulations in this study. It is to be noted that the melting without electric field produced time independent results even at a large time step size of 0.1 s. However, to ensure the stability of the convection dominant hyperbolic charge conservation equation and the time step independence for unsteady flow patterns, a much smaller time step size of 0.001 s is required.

4. Results and discussion

Results of the present numerical analysis on melting of a PCM in a shell-and-tube LHTES unit assisted with EHD flow are presented in this section. All the simulations are carried out up to a physical time of 3600 s. The effects of applied electric field strength and the orientation of the LHTES unit are analyzed. The applied voltage is varied from 0 to 10 kV in steps of 2. It is to be noted that the occurrence of charge injection at $V_0 \leq 2$ kV is not guaranteed. Thus, the results provided for $V_0 = 2$ kV is only for reference. The occurrence of charge injection at $V_0 = 2$ kV is subjected to experimental verification. The transient dynamics of the melting process in the presence of charge injection is explained in Section 4.1. The melt interface progress and the flow structure influenced by the applied electric field is presented in Section 4.2. The melting performance of the shell-and-tube LHTES unit in the presence of EHD flow is quantified in terms of charging time and power storage in Section 4.3.

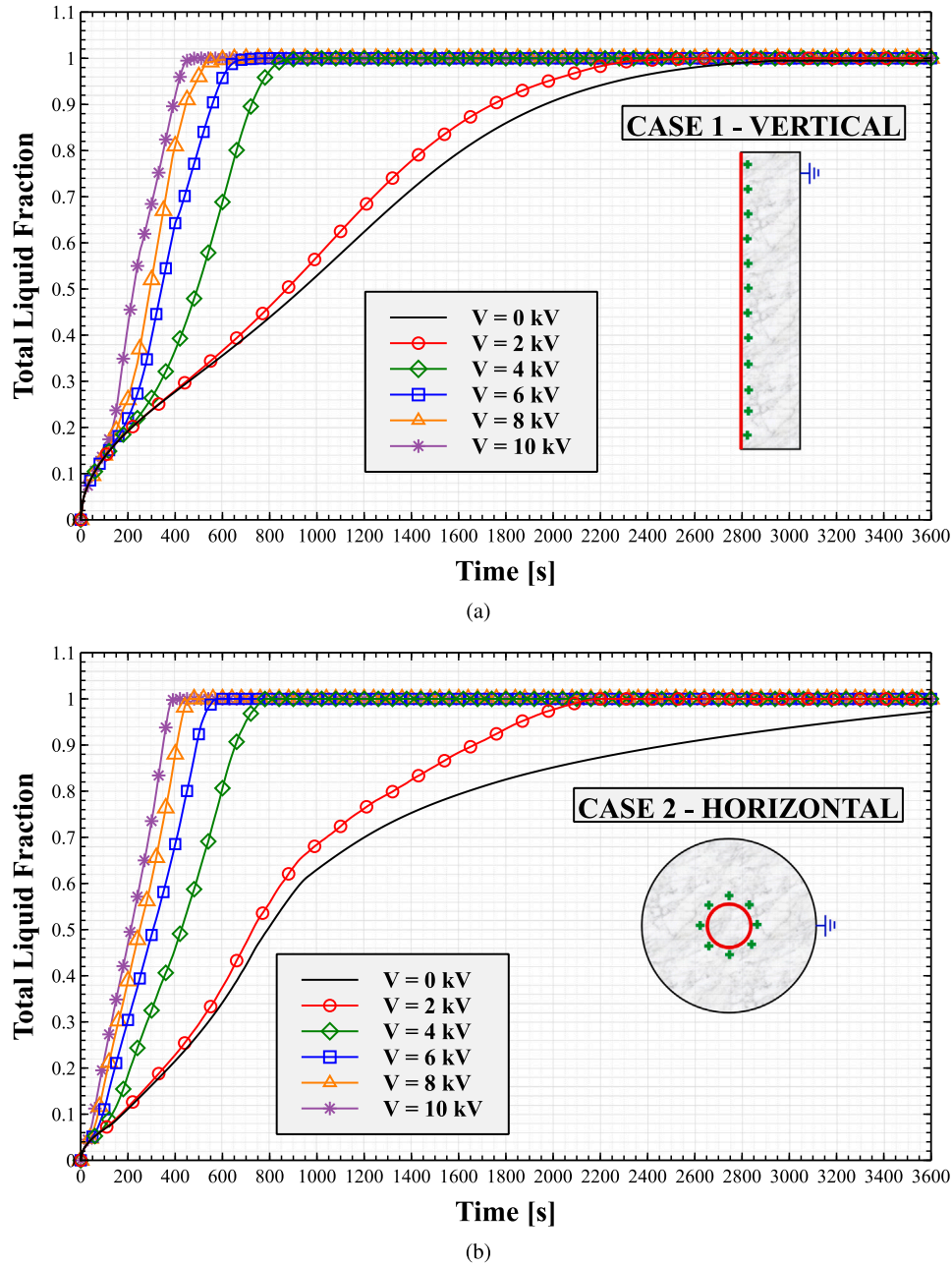


Fig. 5. Time evolution of total liquid fraction in the computational domain at $0 \leq V_0 \leq 10$ kV in (a) Case 1: Vertical orientation and (b) Case 2: Horizontal orientation.

4.1. Melting dynamics in the presence of electric field

The time evolution curves of the total liquid fraction in the computational domain for the vertical (case 1) and horizontal (case 2) orientations of the LHTES unit at $0 \leq V_0 \leq 10$ kV are presented in Figs. 5(a) and 5(b), respectively. At time $t = 0$, the domain is filled with solid PCM and the total liquid fraction in the computational domain is zero. In the absence of electric field ($V_0 = 0$), the total liquid fraction begins to increase due to the heating from the tube surface. As time progresses, the rate of melting slows down and the slope of the melting curve begins to decrease. Finally, the melting curve gets saturated as the total liquid fraction in the computational domain approaches to 1. It is to be noted that the maximum value of total liquid fraction achieved in 3600 s for case 1 without electric field is 0.995 (99.5%), whereas, the same for case 2 is only 0.9722 (97.2%). This can be attributed to the conduction dominated melting in the bottom half of the domain in the horizontal orientation (case 2). In the vertical orientation, the

natural convection flow influences the entire domain. Whereas in the horizontal orientation, the natural convection is dominant only in the region above the heated tube surface and the melting process in the region below the tube surface is primarily due to the conduction heat transfer. In the presence of electric field ($V_0 > 0$ kV), the melting rate curve is coincident with that of the case without electric field ($V_0 = 0$ kV) in the initial stages of melting. This period marks the conduction dominated melting process. At the early stages, the total liquid fraction in the computational domain is less and thus, the fluid motion is not significant. Hence, the heat transfer is primarily due to conduction. Therefore, the melting rate curves of $V_0 > 0$ kV are coincident with that of $V_0 = 0$ kV. However, with further progress of time, the total liquid fraction in the domain gets higher, which enables the fluid motion. At this stage, the melting curves for the cases with $V_0 > 0$ kV begin to deviate from the curve for the case without electric field. This deflection point denotes the onset of EHD flow due to the electric field. The EHD flow induced by charge injection increases the convection heat transfer,

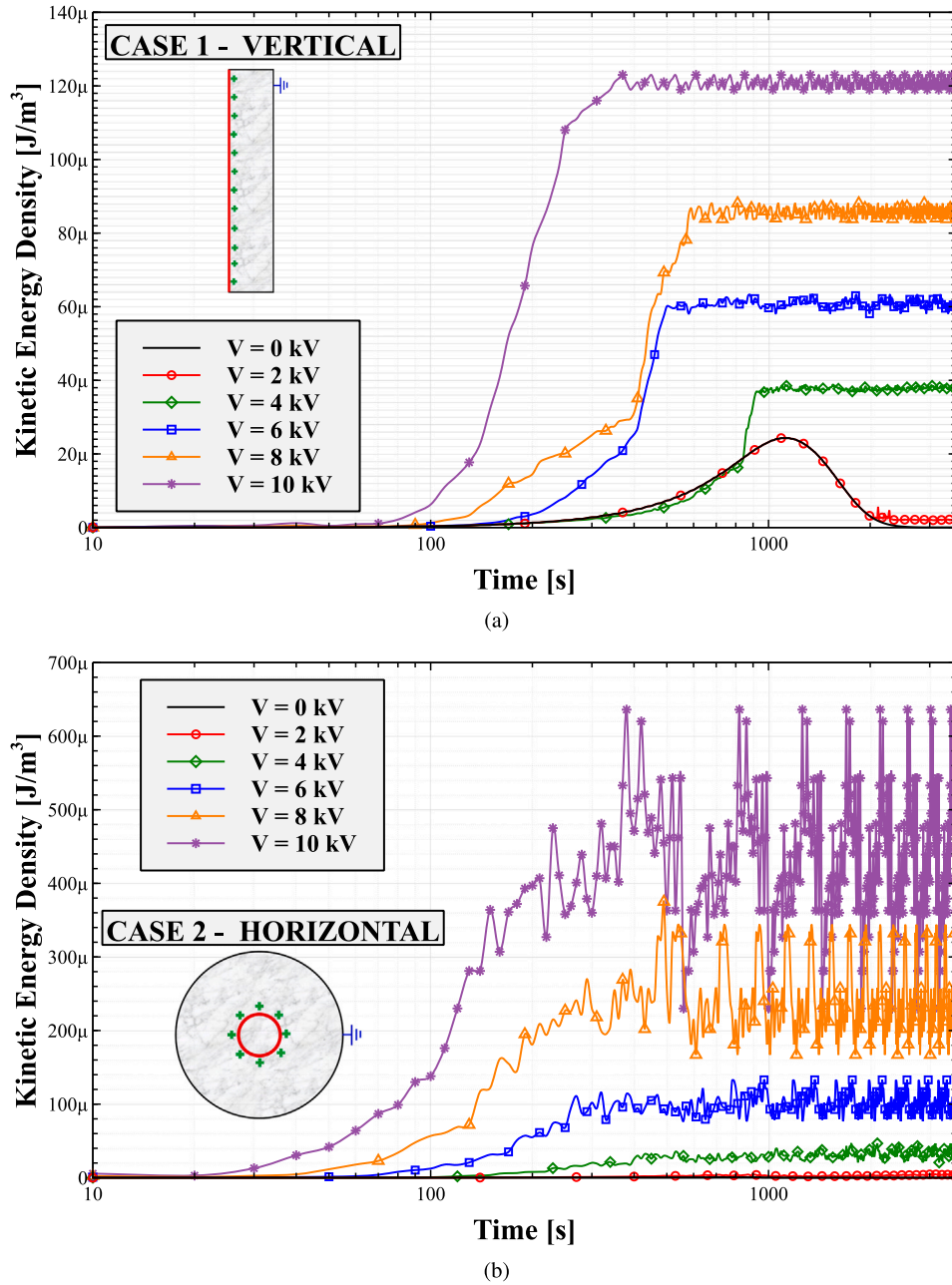


Fig. 6. Time evolution of kinetic energy density in the liquid region of the computational domain at $0 \leq V_0 \leq 10$ kV in (a) Case 1: Vertical orientation and (b) Case 2: Horizontal orientation.

thereby, increasing the melting rate. This deflection point occurs earlier for higher applied voltages. From Fig. 5, it is noticed that the melting rate is much higher for the cases with electric field as compared to the benchmark case without electric field. The increase in melting rate is marginally higher for the cases with $V_0 = 2$ kV. However, for the cases with $V_0 \geq 4$ kV, the slopes of the melting rate curves are steep denoting a notable enhancement in melting speed.

In order to further explore the melting dynamics in the presence of electric field, the evolution of kinetic energy density in the computational domain is presented in Fig. 6. The instantaneous kinetic energy density in the domain is calculated as follows [58]:

$$\text{Kinetic energy density } KE = \frac{1}{v_f} \int_{v_f} \vec{u}^2 dv \quad (9)$$

Here, v_f is the volume of the liquid PCM in the computational domain. Kinetic energy density in the fluid domain is a measure for the

intensity of fluid motion in the liquid domain. Higher values of kinetic energy density indicates stronger fluid motion and vice versa. In other words, the kinetic energy density of a fluid is an important factor in determining the potential for energy conversion in fluid flow systems. The evolution curves of KE with respect to time for cases 1 and 2 and applied voltage $0 \leq V_0 \leq 10$ kV are presented in Figs. 6(a) and 6(b). The kinetic energy density in the domain is close to zero in the initial stages of melting. This period marks the conduction dominated region where the melting rate curves of cases with $V_0 = 0$ kV are coincident with those of $V_0 > 0$ kV. With the progress of time, the KE curve becomes non-zero marking the onset of fluid motion. For $V_0 = 0$ kV, the onset of fluid motion occurs slower than the cases with electric field. The onset of fluid motion for $V_0 = 0$ and 2 kV occurs more or less at the same time. This indicates that the effect of electric field on onset of fluid motion is weak at $V_0 = 2$ kV. However, the onset of fluid motion for $V_0 \geq 4$ kV occurs earlier for higher applied voltages for both cases

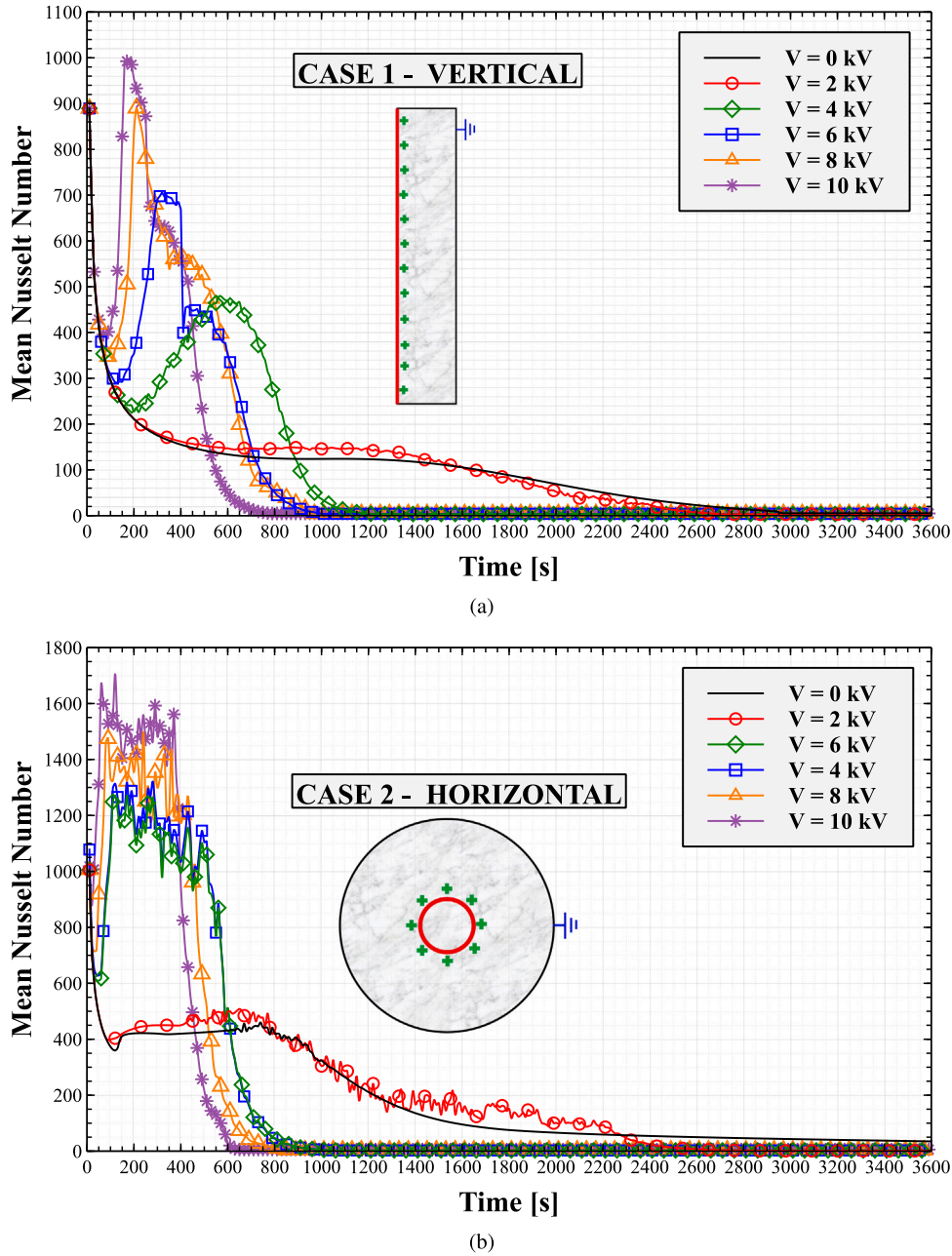


Fig. 7. Time evolution of mean Nusselt number along the hot tube surface at $0 \leq V_0 \leq 10$ kV in (a) Case 1: Vertical orientation and (b) Case 2: Horizontal orientation.

1 and 2. For $V_0 = 0$ and 2 kV, the kinetic energy density increases for a while, then falls gradually and reaches a steady value, in case 1. The onset of fluid motion increases the kinetic energy density in the domain. But, the increase in liquid volume with respect to time leads to the fall of KE . At $V_0 \leq 2$ kV, the curves of KE are almost coincident except of the marginal difference in the end of melting process. This confirms that the raise in kinetic energy density is mainly due to the natural convective flow motion which is not strong enough to sustain the growth in KE with the increase in liquid volume. In case 2, the KE curve shows only a marginal increase to a non-zero value after the onset of fluid motion for $V_0 = 0$ and 2 kV. The bump in KE curve as observed at $V_0 \leq 2$ kV in case 1 is not seen in case 2. This indicates that both natural convective flow motion and the EHD flow motion are weak in horizontal configuration at $V_0 \leq 2$ kV. For both cases 1 and 2, the increase in KE is notably high after the onset of fluid motion at applied voltages greater than or equal to 4 kV. This confirms that the application of electric field leads to stronger fluid

motion in the melted PCM region. For $V_0 \geq 4$ kV, the KE curves begins to exhibit strong periodic oscillations after the point where 100% melting is achieved. The random oscillations with respect to time observed in the KE indicate that the EHD flow motion induced by charge injection is chaotic in nature. This can be attributed to the high values (> 2000) of electric Rayleigh number $T = \frac{\epsilon_l V_0}{\mu K_l}$. The EHD flow at higher electric Rayleigh numbers are characterized by random chaotic flow vortices [52,59]. As the melting approaches 100%, the flow field in the computational domain becomes same as the chaotic flow regime experienced in a single-phase fluids at strong electric fields. Unlike the curves of $V_0 = 0$ and 2 kV, the strong electroconvective flow induced by the charge injection helps to sustain the high values of KE until the end of simulation up to 3600 s. Furthermore, the amplitude of oscillations is higher in case 2 than case 1, because the influence of buoyancy force is weaker in horizontal orientation. Thus, the electroconvective motion is stronger and exhibits more chaotic flow patterns. In overall, it can be inferred that the application of electric field leads to earlier onset

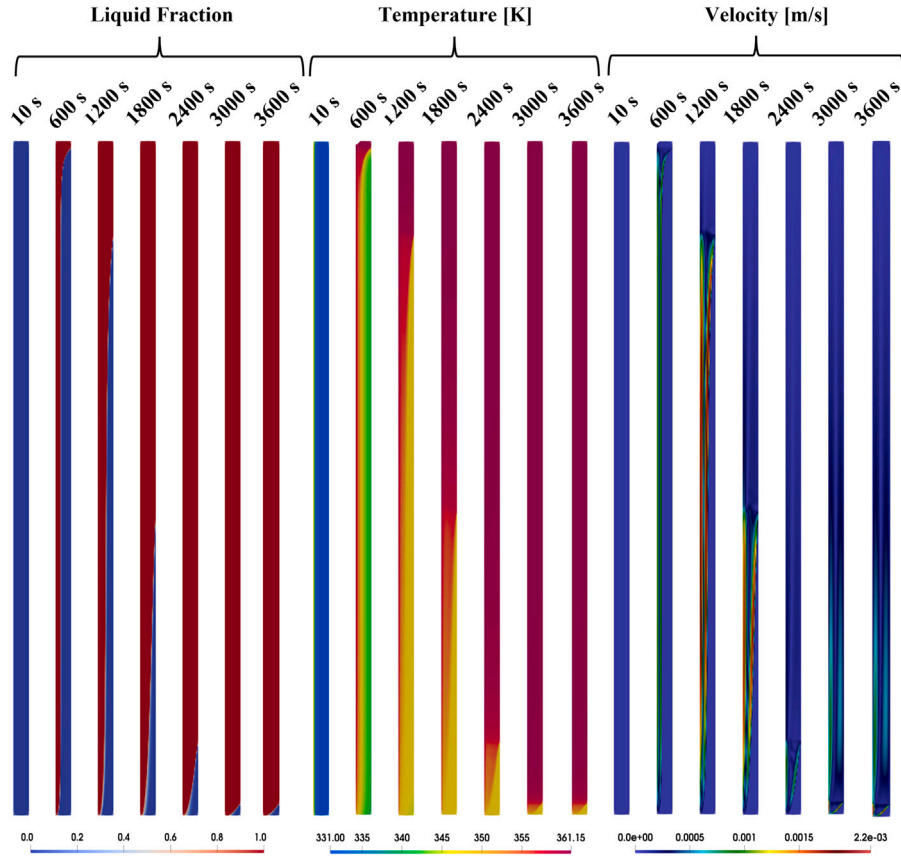


Fig. 8. Contours of liquid fraction, temperature and velocity at different instantaneous time moments in vertical orientation (case 1) at an applied voltage $V_0 = 0$ kV.

of fluid motion and generates random chaotic EHD flow vortices in the liquid region. This leads to increased velocity distribution, mixing and heat transfer resulting in faster melting rates as observed in Fig. 5.

The time variation of the mean Nusselt number (Nu_M) along the tube surface for both the cases 1 and 2 at $0 \leq V_0 \leq 10$ kV are presented in Figs. 7(a) and 7(b), respectively. The mean Nusselt number Nu_M is defined as the surface weighted average of the local Nusselt number (Nu) along the hot surface. Local Nusselt number is calculated as $Nu = -\frac{\partial T}{\partial y} \frac{L}{\theta_H - \theta_{\infty}}$. Where, L is the length of the hot surface (height of tube in case 1 and diameter of tube in case 2). For the cases without electric field ($V_0 = 0$ kV), the mean Nusselt number initially experiences a drop and then remains constant for a while and then gradually decreases and finally gets saturated at a constant value. The initial drop marks the conduction dominated region and then the constant plateau marks the sustained fluid motion regime due to natural convection. Once the melting is about to be complete, the mean Nusselt number begins to fall due to the raise in temperature in the liquid region. Finally, when the melting is more than 90%, the mean Nusselt number reaches a constant value due to the thermal stratification. For the cases with $V_0 = 2$ kV, the behavior is synonymous with only a marginal increase in the mean Nusselt number distribution. This indicates that the heat transfer enhancement at $V_0 = 2$ kV is only slightly higher than the benchmark case without electric field. This can also be related to the liquid fraction and KE curves of $V_0 = 2$ kV presented in Figs. 5 and 6. In contrast, the cases with $V_0 \geq 4$ kV show a significantly higher mean Nusselt number distribution in the plateau region. This period marks the strong electroconvective flow motion that leads to enhanced heat transfer. The peak value of the mean Nusselt number distribution gets higher with increasing applied voltages. Furthermore, the time variation of mean Nusselt number for the cases with electric field is characterized with random chaotic oscillations. This observation can be related to the random oscillations in the KE curves (refer Fig. 6) that mark the

chaotic vortices generated in EHD flows with high electric Rayleigh numbers. It is to be noted that the mean Nusselt number curves for the cases with electric field ($V_0 > 0$ kV) reach thermal stratification much earlier than the benchmark case without electric field. The melting process gets completed much earlier in the presence of electric field and therefore, the system also reaches earlier thermal stratification. The final mean Nusselt number in stratified state for the cases with electric field are also marginally lower than the cases without electric field. This is because, for the cases without electric field, the total liquid fraction is less than 100% at 3600 s. But, the cases with electric field reach 100% melting at a much shorter time period.

4.2. Flow and melt interface morphology

Contours of liquid fraction, temperature and velocity distribution in the vertical orientation (case 1) for $V_0 = 0$ and 10 kV are presented in Figs. 8 and 9, respectively. The key feature to be noted is that the case without electric field does not reach 100% melting even at the end of simulation at 3600 s. Whereas, the case with electric field ($V_0 = 10$ kV) has reached 100% melting at 480 s. Thus, it is obvious that the presence of EHD flow induced by charge injection has led to a notable decrease in melting time. The melting starts from the heated tube surface and progresses towards the shell wall. In the absence of electric field, the melt interface progresses faster in the upper end of the domain and lags behind in the lower end of the domain. This can be attributed to the movement of hotter liquid in the upward direction due to buoyancy effect. Thus, the melt interface is inclined towards the shell wall in the upper part, as influenced by the uni-cellular natural convective fluid motion. The temperature field also takes a similar shape as dictated by the natural convective flow cell. This can be clearly seen in the velocity contour with a single large natural convective flow vortex. However, in the case of $V_0 = 10$ kV, the melt interface take the shape

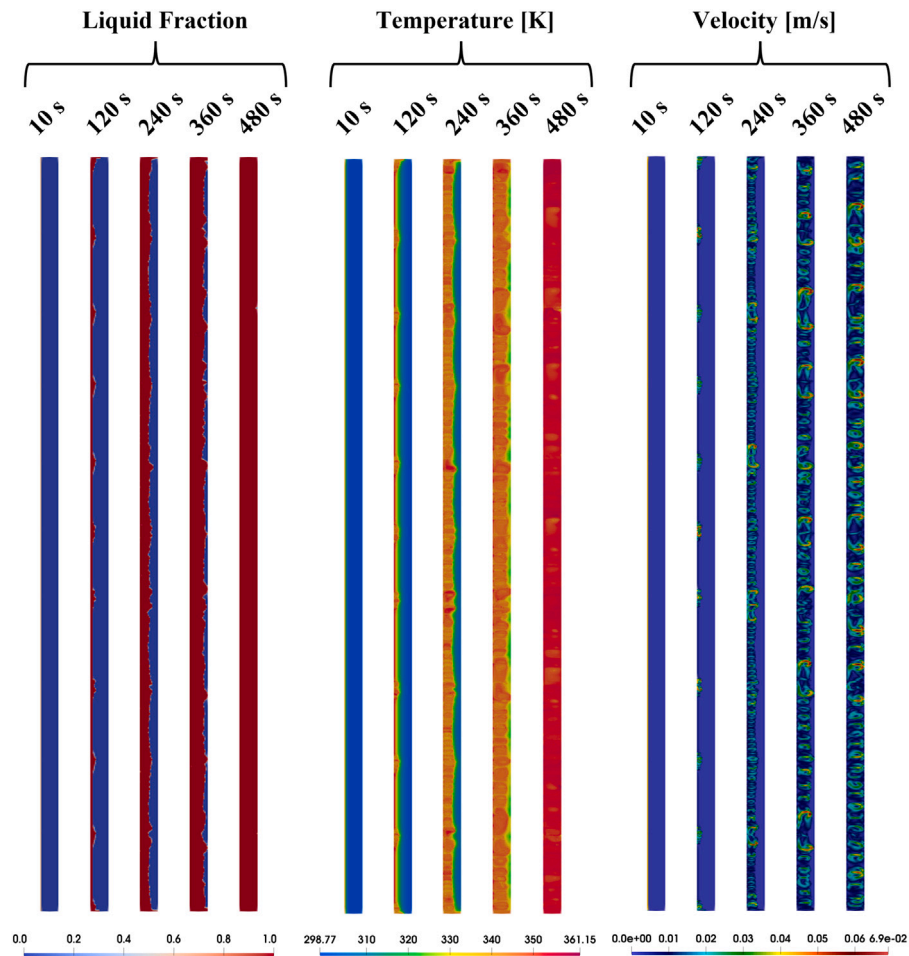


Fig. 9. Contours of liquid fraction, temperature and velocity at different instantaneous time moments in vertical orientation (case 1) at an applied voltage $V_0 = 10$ kV.

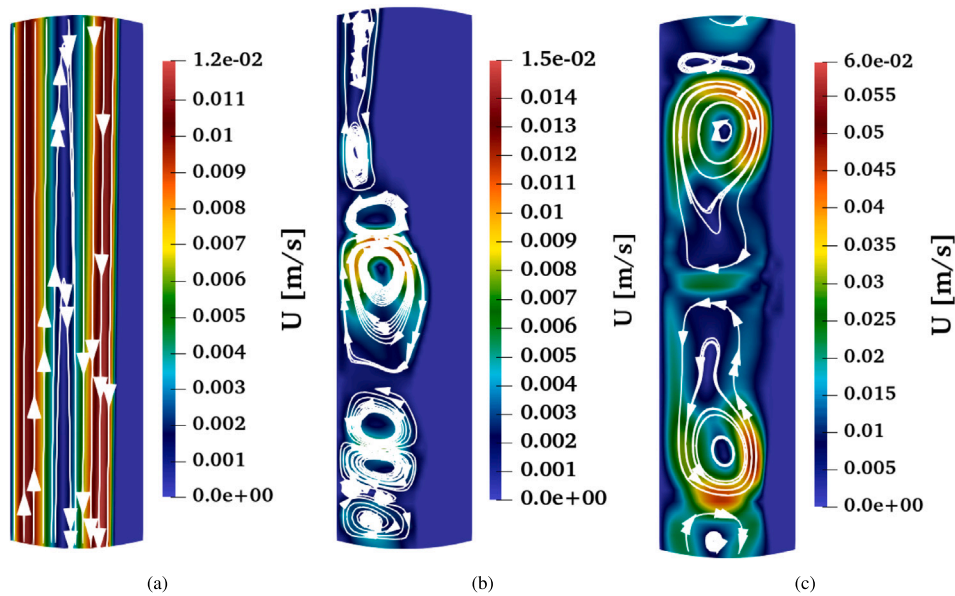


Fig. 10. Zoomed view of the flow field and streamlines in case 1 (vertical orientation) at (a) $V_0 = 0$ kV, (b) $V_0 = 6$ kV and (c) $V_0 = 10$ kV.

of electroconvective flow vortices generated by the charge injection. At $t = 120$ s, the EHD flow vortices (refer velocity contours in Fig. 9) generated from the emitter electrode (tube surface) are noticed. Unlike the case without electric field, the melt interface at $V_0 = 10$ kV takes

the shape of the EHD flow vortices. As the EHD flow gets stronger, the melt interface and temperature contours are completely dictated by the EHD flow cells. Likewise, the peak velocity distribution is also an order of magnitude higher in the case with $V_0 = 10$ kV, as compared to

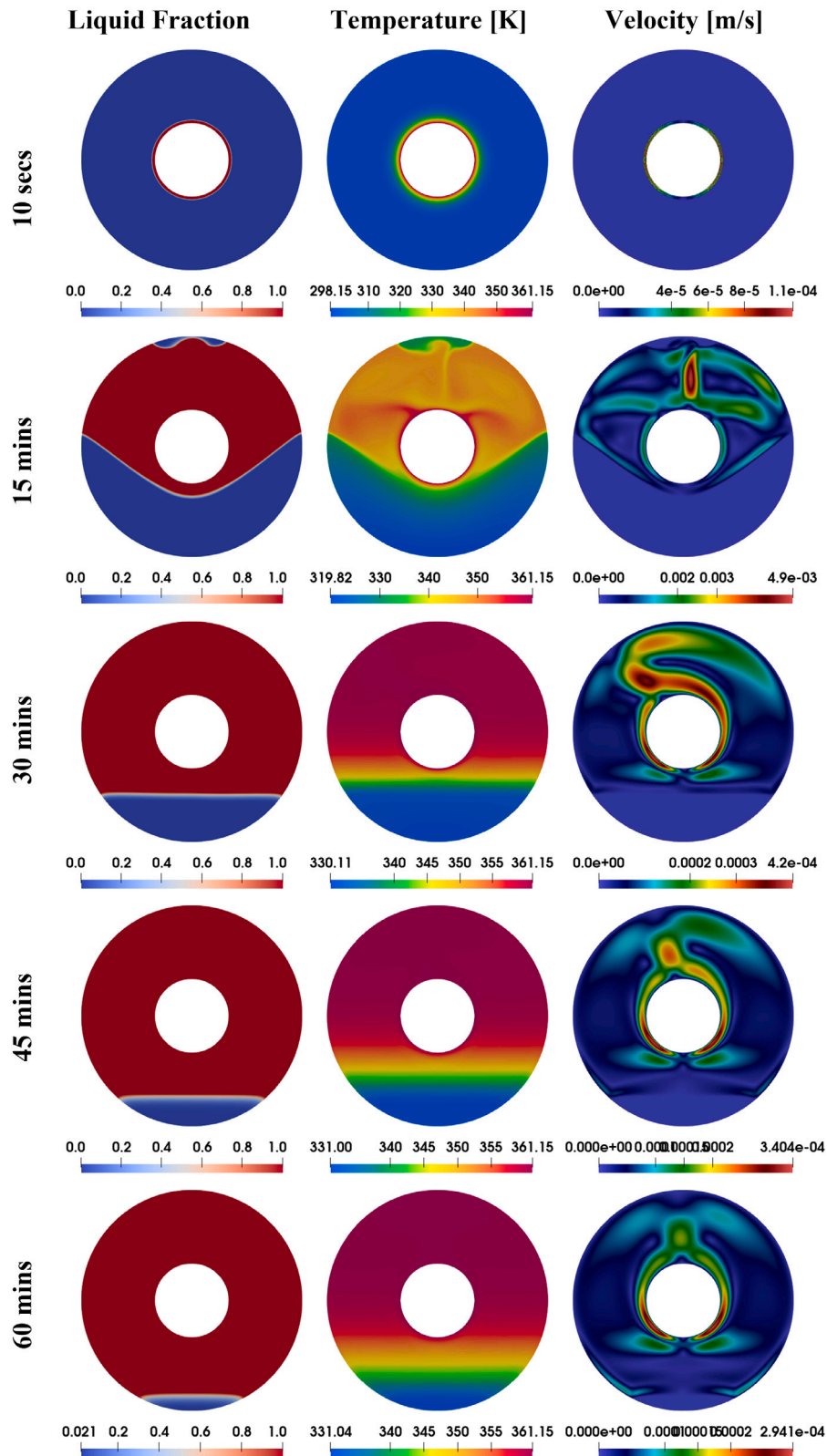


Fig. 11. Contours of liquid fraction, temperature and velocity at different instantaneous time moments in horizontal orientation (case 2) at an applied voltage $V_0 = 0$ kV.

the case without electric field. To provide further insights on the flow morphology in case 1 with and without electric field, a zoomed view of velocity contours with streamlines in the mid-section of the LHTES unit is provided in Fig. 10. The case without electric field is characterized by a smooth velocity distribution and perfectly parallel flow streamlines of

the natural convective flow cell. On the other hand, the flow field in the presence of electric field ($V_0 = 4, 10$ kV) is characterized by multiple flow cells with rotating vortices.

Likewise, the distribution of liquid fraction, temperature and velocity for case 2 with $V_0 = 0$ and 10 kV are presented in Figs. 11 and

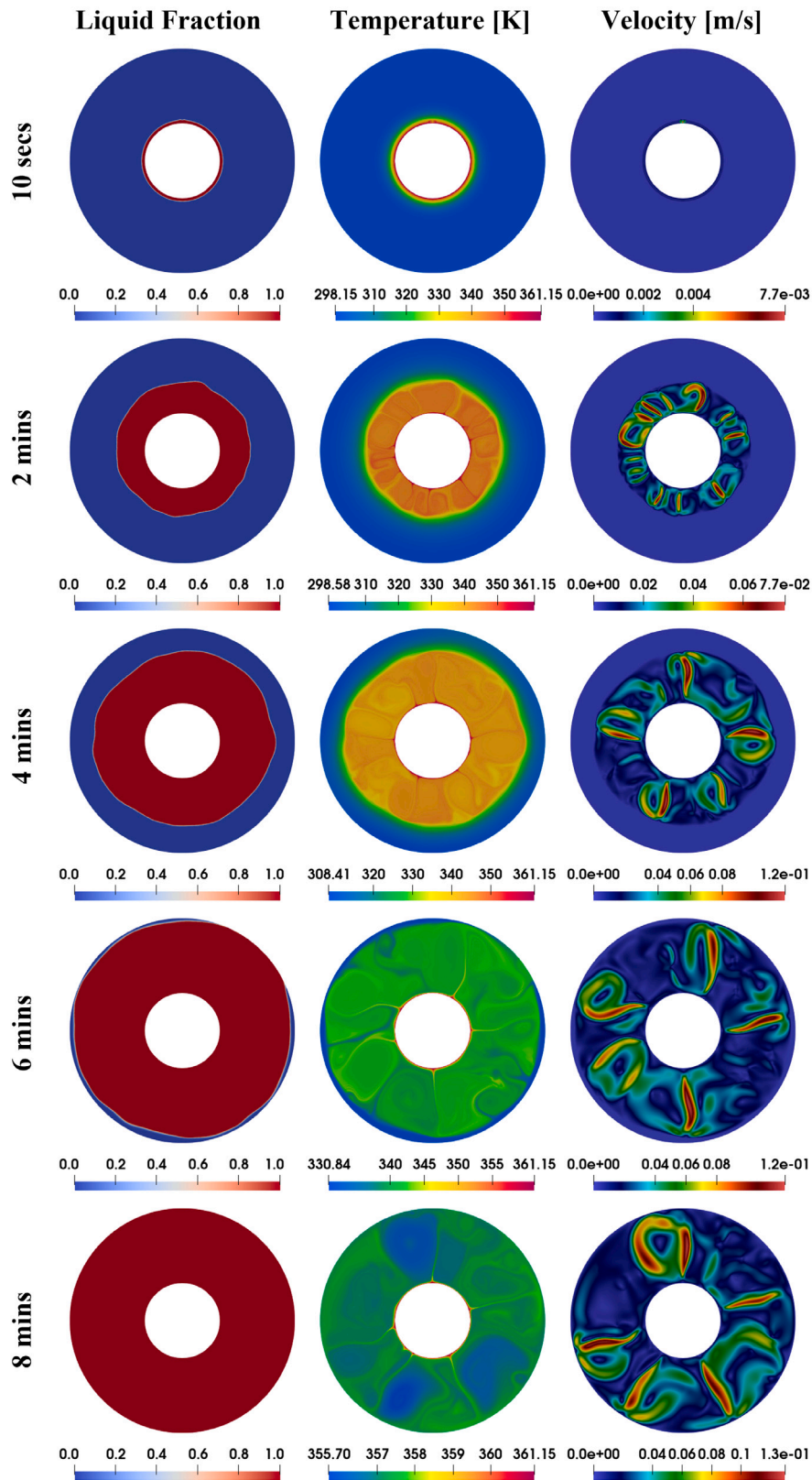


Fig. 12. Contours of liquid fraction, temperature and velocity at different instantaneous time moments in horizontal orientation (case 2) at an applied voltage $V_0 = 10$ kV.

12, respectively. As observed in case 1, the melting does not reach 100% by 3600 s for case 2 without electric field. While, the case with $V_0 = 10$ kV reaches 100% melting at a short time of 8 min. Thus, it is confirmed that the rate of melting is notably enhanced by the charge

injection induced EHD flow. For the case without electric field, it is noted that the melting progress faster in the region above the heated tube. As the hot fluid moves upward due to the buoyancy force, the melt interface progresses faster in the region above the heated tube.

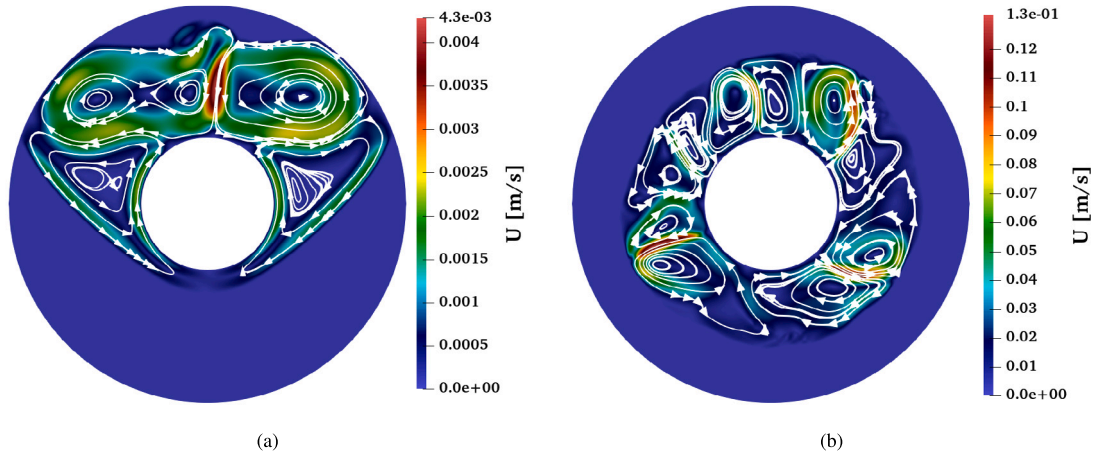


Fig. 13. Zoomed view of the flow field and streamlines in case 2 (horizontal orientation) at (a) $V_0 = 0$ kV and (b) $V_0 = 10$ kV.

Whereas, the melting process in the region below the hot tube is mainly due to the heat conduction. Thus, the progress of melt interface is slower and becomes perfectly horizontal in the region below the heated tube. This observation is also noted in the thermal field. In the initial stages, the melting happens in the upper part of the domain due to natural convective flow motion. This period is marked with natural convective thermal plumes in the upward direction emanating from the heated tube surface. Once the melting gets completed in the upper part of the domain, the melting in the bottom part is purely conduction dominated. Thus, the thermal plumes disappear and the temperature distribution becomes smooth as observed in conduction heat transfer. The velocity field characterized by two or four flow cells that are more or less symmetric about the heated tube. In the case with electric field ($V_0 = 10$ kV), the melt interface progresses almost uniformly around the heated tube. This can be attributed to the EHD flow that is generated uniformly all around the emitter electrode (heated tube). As observed in the velocity contours of Fig. 12, random EHD flow vortices gets developed all around the heated tube. Thus, the heat transfer is primarily dictated by these EHD flow cells. Hence, the melt interface and the thermal field take the shape of the EHD flow cells. Velocity contours with streamlines for case 2 at $V_0 = 0$ and 10 kV are presented in Fig. 13. The flow in the absence of electric field is characterized four flow cells generated due to natural convection. These 4 cells are confined to the region above the heated tube. Whereas, the case with $V_0 = 10$ kV exhibits multiple flow cells generated by charge injection. These randomly oscillating flow cells are approximately uniformly distributed all around the heated tube (emitter electrode).

4.3. Performance evaluation

Finally, the melting performance of the shell-and-tube LHTES unit in the vertical (case 1) and horizontal (case 2) orientations at $0 \leq V_0 \leq 10$ kV are quantified in terms of charging time and total power storage in this section. The variation of charging time for cases 1 and 2 with respect to the applied voltage ($0 \leq V_0 \leq 10$ kV) are presented in Fig. 14. The charging time is defined as the total time required to 97% melting. For the benchmark case without electric field, the total charging time for case 2 is notably higher than that required for case 1. This is due to the fact that the melting in case 2 without electric field is purely conduction drive in the bottom half of the domain. However, in the presence of electric field, the charging time is notably reduced in both the cases. It is worthy to mention that the charging time becomes lower for case 2 than case 1, in the presence of electric field. The percentage reduction in charging time for all the simulation cases considered herein are presented in Fig. 15. The percentage reduction in charging time for case 2 is slightly higher than case 1. The strength of natural convection is higher in case 1 as compared to case 2. Thus, the

influence of EHD flow motion is a bit weaker in case 1, as compared to case 2. Therefore, the net reduction in charging time observed in case 2 is slightly higher than that of case 1.

The total power stored in the shell-and-tube LHTES unit is defined as [60]

$$\text{Total stored power } P = \frac{[m_l \cdot (C_{p,l} \cdot (\theta_l - \theta_\infty) + L)] + [m_s \cdot C_{p,s} \cdot (\theta_s - \theta_\infty)]}{\text{Time required to reach 97\% melting}} \quad (10)$$

Here, m_l and m_s denote the mass of liquid and solid PCM when 97% melting is reached. θ_l and θ_s are the mean liquid and solid temperatures at 97% melting. In the above expression, the first term in the numerator represents the total heat content stored in the liquid PCM. Where, $m_l \cdot (C_{p,l} \cdot (\theta_l - \theta_\infty))$ indicate the sensible heat content used to raise the temperature of the liquid PCM and $m_l \cdot L$ is the latent heat component of the energy stored during the melting process. Likewise, the second term in the numerator represents the sensible heat content stored in the solid PCM. The total power stored at 97% melting in case 1 and 2 are presented in Figs. 16(a) and 16(b). It is evident that the net power stored increases with the increase in applied voltage. The maximum increase in net power storage for case 1 is around 80.85%. Whereas, a maximum of 88.35% increase in total power stored is noted in case 2. This confirms that the effect of electric field induced flow motion on melting performance is higher in case 2 than case 1. The additional electric power consumption to generate the EHD vortices can be evaluated by $P_{EL} = V \times I_{tot}$, where I_{tot} represents the total electric current in the system. The total electric current in the system at a given instantaneous moment is estimated as:

$$I_{tot} = \iint \vec{J} \cdot \hat{n} dS \quad (11)$$

The mean total electric current for a period of 3600 s through the electrode surface calculated as per Eq. (11) vary approximately from 2 to 7 μA . The maximum electric power consumption calculated based on the mean total electric current at $V_0 = 10$ kV for case 1 is 13.42×10^{-3} W and for case 2 is 2.179×10^{-4} W. Thus, active vortex generation by charge injection can produce significant enhancement in melting performance of a shell-and-tube LHTES module with only a few milliwatts of additional electric power consumption. Results of this study indicate that active vortex generation using charge injection is an viable and economic melting performance enhancement technique in a shell-and-tube latent heat thermal energy storage (LHTES) unit.

5. Concluding remarks

This study proposed a shell-and-tube LHTES design assisted with active vortex generation by charge injection for melting performance

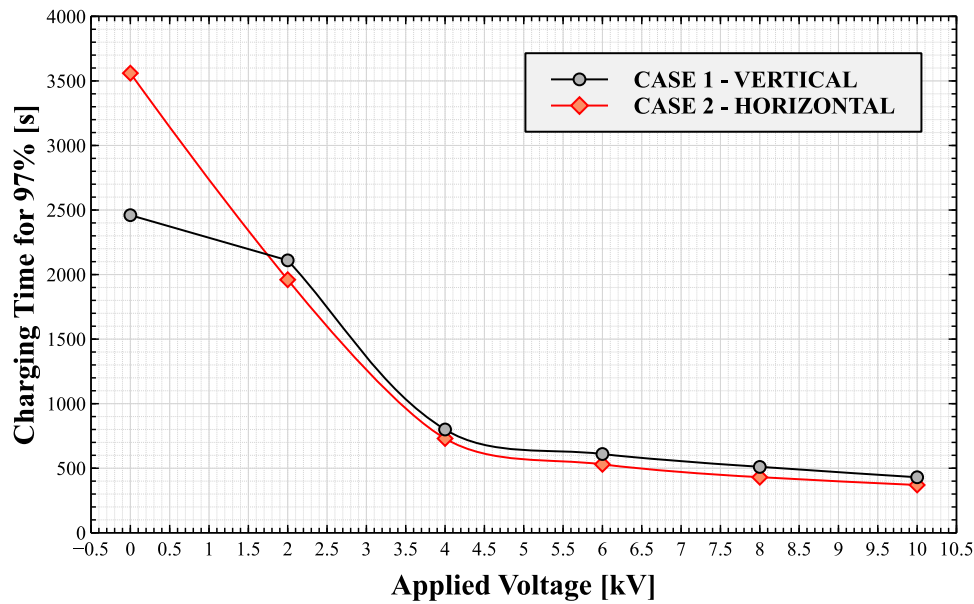


Fig. 14. Charging time required to reach 97% melting in vertical (case 1) and horizontal (case 2) orientations at $0 \leq V_0 \leq 10$ kV.

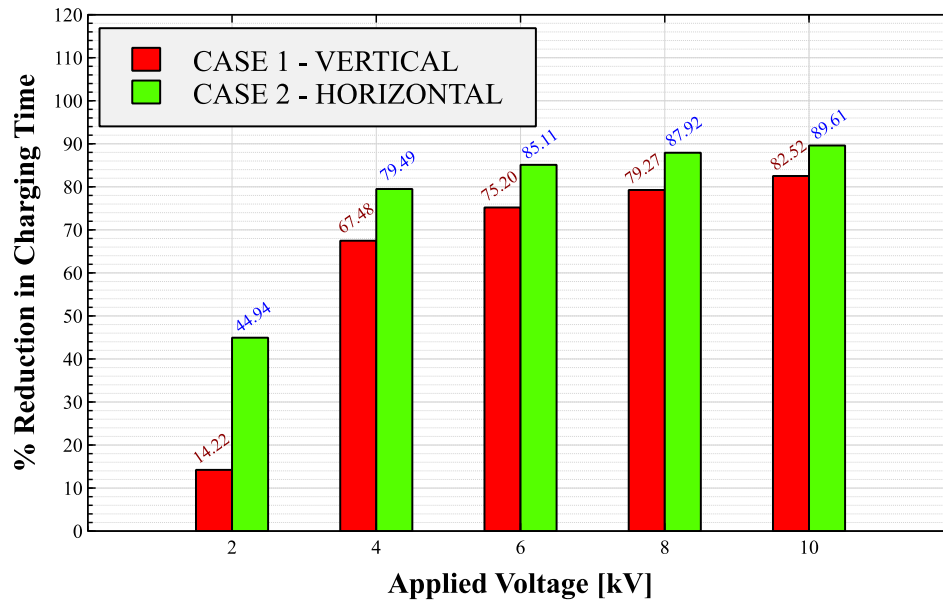


Fig. 15. Percentage reduction (with reference to case without electric field) in charging time required to reach 97% melting in vertical (case 1) and horizontal (case 2) orientations at $2 \leq V_0 \leq 10$ kV.

enhancement. A 2D numerical analysis in both vertical and horizontal configurations of the LHTES unit are performed. The melting performance at 6 levels of applied voltages in both the vertical and horizontal configurations are studied. The transient melting dynamics in the shell-and-tube LHTES unit in the presence of electrohydrodynamic (EHD) flow is mapped with respect to time in terms of total liquid fraction, kinetic energy density and mean Nusselt number. The flow and interface morphology are highlighted by contours of liquid fraction, temperature and velocity contours. The melting performance is quantified in terms of total charging time and net power stored. Key findings of this study are summarized below:

- Charge injection generates multiple flow vortices from the emitter electrode (heated tube) surface.
- EHD flow vortices alter the flow structure, increase flow strength, mixing and heat transfer in the fluid region.
- The melt interface takes the shape of the vortices generated by charge injection.
- In the vertical orientation (case 1), the EHD flow makes the melting uniform in the top and bottom parts of the LHTES unit.
- In the horizontal orientation (case 2), the EHD flow makes the melting uniform all around the heated tube.
- A maximum of 82.52% and 89.61% reduction in total charging time is observed at cases 1 and 2, respectively.
- A maximum of 80.85% and 88.35% increase in total power stored in the LHTES unit is noted in cases 1 and 2, respectively.
- The performance enhancement by EHD flow is slightly more effective in case 2 due to the weaker buoyancy force.
- The maximum additional electric power consumption is in the order of few milliwatts (13 mW for case 1 and 0.2 mW for case 2).

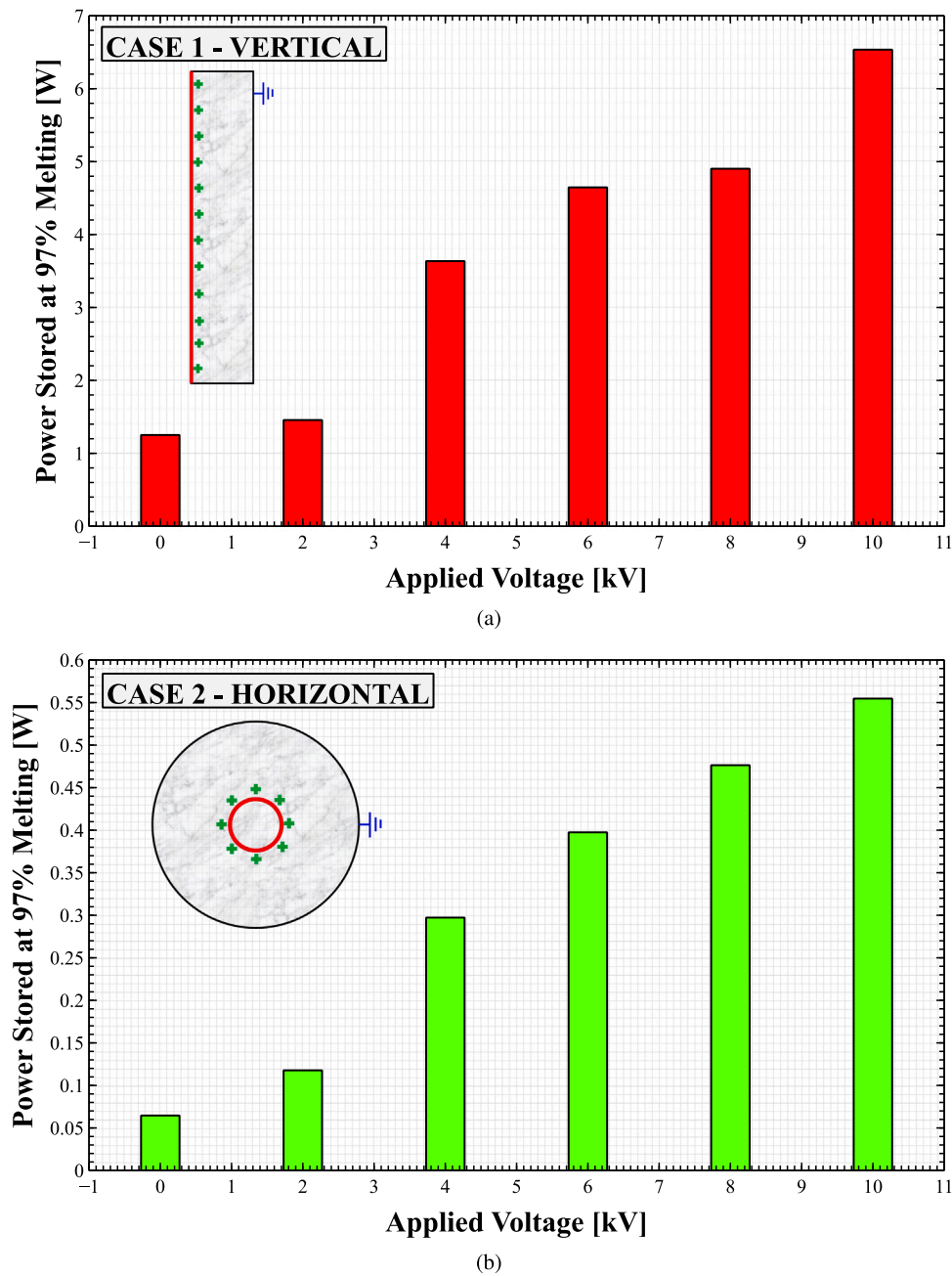


Fig. 16. Total power stored in the PCM at 97% liquid fraction for (a) Case 1: Vertical orientation and (b) Case 2: Horizontal orientation, at different applied voltages ($0 \leq V_0 \leq 2$ kV).

Thus, EHD flow based melting enhancement is a potential technique with simple design and notable performance improvement with minimal additional electric power consumption.

Results presented in this study give deeper insights on the mechanism of melting performance enhancement in a shell-and-tube LHTES unit by EHD flow generated by charge injection. The results indicate that the active vortex generation by electric field induced charge injection is an effective and economic technique to enhance melting performance in a shell-and-tube LHTES module. The authors propose to extend this research to further complex 3D LHTES designs with different electrode configurations and fluid flow directions.

CRediT authorship contribution statement

R. Deepak Selvakumar: Conceptualized, Implemented the governing equations in OpenFOAM, Performed the simulations, Writing

– original draft. **Jian Wu:** Formal analysis. **Imran Afgan:** Writing – review & editing. **Yulong Ding:** Writing – review & editing. **Ahmed K. Alkaabi:** Supervision.

Declaration of competing interest

The authors declare that they have no known competing financial interests or personal relationships that could have appeared to influence the work reported in this paper.

Data availability

The authors are unable or have chosen not to specify which data has been used

Acknowledgments

This research work is supported by Khalifa University of Science and Technology (KUST), United Arab Emirates under Award No. CIRA-2021-066. The authors acknowledge the support from Emirates Nuclear Technology Center (ENTC), United Arab Emirates and the computational resources provided by the Research Computing Center, KUST, United Arab Emirates. One of the author acknowledges the support from National Natural Science Foundation of China - NSFC (11802079).

References

- [1] S.Y. Abujarad, M.W. Mustafa, J.J. Jamian, Recent approaches of unit commitment in the presence of intermittent renewable energy resources: A review, *Renew. Sustain. Energy Rev.* 70 (2017) 215–223.
- [2] T.E. Rehm, Advanced nuclear energy: the safest and most renewable clean energy, *Cur. Opin. Chem. Eng.* 39 (2023) 100878.
- [3] R. Loisel, V. Alexeeva, A. Zucker, D. Shropshire, Load-following with nuclear power: Market effects and welfare implications, *Prog. Nucl. Energy* 109 (2018) 280–292.
- [4] F. Tooryan, H. HassanzadehFard, E.R. Collins, S. Jin, B. Ramezani, Smart integration of renewable energy resources, electrical, and thermal energy storage in microgrid applications, *Energy* 212 (2020) 118716.
- [5] Y. Tian, C.-Y. Zhao, A review of solar collectors and thermal energy storage in solar thermal applications, *Appl. Energy* 104 (2013) 538–553.
- [6] T. Okazaki, Y. Shirai, T. Nakamura, Concept study of wind power utilizing direct thermal energy conversion and thermal energy storage, *Renew. Energy* 83 (2015) 332–338.
- [7] M. Ali, A.K. Alkaabi, J.I. Lee, CFD simulation of an integrated PCM-based thermal energy storage within a nuclear power plant connected to a grid with constant or variable power demand, *Nucl. Eng. Des.* 394 (2022) 111819.
- [8] M. Ali, A.K. Alkaabi, Y. Addad, Numerical investigation of a vertical triplex-tube latent heat storage/exchanger to achieve flexible operation of nuclear power plants, *Int. J. Energy Res.* 46 (3) (2022) 2970–2987.
- [9] N. Zhang, Y. Yuan, X. Cao, Y. Du, Z. Zhang, Y. Gui, Latent heat thermal energy storage systems with solid-liquid phase change materials: A review, *Adv. Eng. Mater.* 20 (6) (2018) 1700753.
- [10] R. Elarem, T. Alqahtani, S. Mellouli, F. Askri, A. Edacherian, T. Vineet, I.A. Badruddin, J. Abdelmajid, A comprehensive review of heat transfer intensification methods for latent heat storage units, *Energy Storage* 3 (1) (2021) e127.
- [11] B.M. Diaconu, M. Cruceru, L. Angheliescu, A critical review on heat transfer enhancement techniques in latent heat storage systems based on phase change materials. Passive and active techniques, system designs and optimization, *J. Energy Storage* 61 (2023) 106830.
- [12] R.P. Singh, S. Kaushik, D. Rakshit, Melting phenomenon in a finned thermal storage system with graphene nano-plates for medium temperature applications, *Energy Convers. Manage.* 163 (2018) 86–99.
- [13] M. Arici, E. Tütüncü, Ç. Yıldız, D. Li, Enhancement of PCM melting rate via internal fin and nanoparticles, *Int. J. Heat Mass Transfer* 156 (2020) 119845.
- [14] A. Acir, M.E. Canli, Investigation of fin application effects on melting time in a latent thermal energy storage system with phase change material (PCM), *Appl. Therm. Eng.* 144 (2018) 1071–1080.
- [15] L. Wu, X. Zhang, X. Liu, Numerical analysis and improvement of the thermal performance in a latent heat thermal energy storage device with spiderweb-like fins, *J. Energy Storage* 32 (2020) 101768.
- [16] J. Li, Y. Huang, C. Zhang, X. Liu, Numerical study on the solidification performance of a latent heat storage unit with Koch-fractal fin, *Fractals* 27 (2019) 1950108.
- [17] R. Qaiser, M.M. Khan, H.F. Ahmed, F.K. Malik, M. Irfan, I.U. Ahad, Performance enhancement of latent energy storage system using effective designs of tubes and shell, *Energy Rep.* 8 (2022) 3856–3872.
- [18] A.M. Abdulateef, S. Mat, J. Abdulateef, K. Sopian, A.A. Al-Abidi, Geometric and design parameters of fins employed for enhancing thermal energy storage systems: A review, *Renew. Sustain. Energy Rev.* 82 (2018) 1620–1635.
- [19] A. Raul, M. Jain, S. Gaikwad, S.K. Saha, Modelling and experimental study of latent heat thermal energy storage with encapsulated PCMs for solar thermal applications, *Appl. Therm. Eng.* 143 (2018) 415–428.
- [20] H. Peng, J. Wang, X. Zhang, J. Ma, T. Shen, S. Li, B. Dong, A review on synthesis, characterization and application of nanoencapsulated phase change materials for thermal energy storage systems, *Appl. Therm. Eng.* 185 (2021) 116326.
- [21] W. Gao, F. Liu, C. Yu, Y. Chen, X. Liu, Microfluidic method-based encapsulated phase change materials: Fundamentals, progress, and prospects, *Renew. Sustain. Energy Rev.* 171 (2023) 112998.
- [22] M. Arici, E. Tütüncü, A. Campo, Numerical investigation of melting of paraffin wax dispersed with CuO nanoparticles inside a square enclosure, *Heat Transfer Res.* 49 (9) (2018).
- [23] N. Abed, I. Afgan, A. Cioncolini, H. Iacovides, A. Nasser, T. Mekhail, Thermal performance evaluation of various nanofluids with non-uniform heating for parabolic trough collectors, *Case Stud. Therm. Eng.* 22 (2020) 100769.
- [24] M. Arici, E. Tütüncü, M. Kan, H. Karabay, Melting of nanoparticle-enhanced paraffin wax in a rectangular enclosure with partially active walls, *Int. J. Heat Mass Transfer* 104 (2017) 7–17.
- [25] N. Abed, I. Afgan, H. Iacovides, A. Cioncolini, I. Khurshid, A. Nasser, Thermal-hydraulic analysis of parabolic trough collectors using straight conical strip inserts with nanofluids, *Nanomaterials* 11 (4) (2021) 853.
- [26] Y. Lin, Y. Jia, G. Alva, G. Fang, Review on thermal conductivity enhancement, thermal properties and applications of phase change materials in thermal energy storage, *Renew. Sustain. Energy Rev.* 82 (2018) 2730–2742.
- [27] M. Aramesh, B. Shabani, Metal foam-phase change material composites for thermal energy storage: A review of performance parameters, *Renew. Sustain. Energy Rev.* 155 (2022) 111919.
- [28] S.C. Costa, M. Kenisarin, A review of metallic materials for latent heat thermal energy storage: Thermophysical properties, applications, and challenges, *Renew. Sustain. Energy Rev.* 154 (2022) 111812.
- [29] G. Wu, S. Chen, S. Zeng, Effects of mechanical vibration on melting behaviour of phase change material during charging process, *Appl. Therm. Eng.* 192 (2021) 116914.
- [30] W. Cui, X. Li, X. Li, L. Lu, T. Ma, Q. Wang, Combined effects of nanoparticles and ultrasonic field on thermal energy storage performance of phase change materials with metal foam, *Appl. Energy* 309 (2022) 118465.
- [31] M. Ghalambaz, S.M.H. Zadeh, S. Mehryan, I. Pop, D. Wen, Analysis of melting behavior of PCMs in a cavity subject to a non-uniform magnetic field using a moving grid technique, *Appl. Math. Model.* 77 (2020) 1936–1953.
- [32] S. Mehryan, A. Tahmasebi, M. Izadi, M. Ghalambaz, Melting behavior of phase change materials in the presence of a non-uniform magnetic-field due to two variable magnetic sources, *Int. J. Heat Mass Transfer* 149 (2020) 119184.
- [33] D. Nakhla, H. Sadek, J.S. Cotton, Melting performance enhancement in latent heat storage module using solid extraction electrohydrodynamics (EHD), *Int. J. Heat Mass Transfer* 81 (2015) 695–704.
- [34] D. Nakhla, Characterization of Electrohydrodynamic (EHD) heat transfer enhancement mechanisms in melting of organic Phase Change Material (PCM) (Ph.D. thesis), McMaster University, 2018.
- [35] D. Nakhla, E. Thompson, B. Lacroix, J. Cotton, Measurement of heat transfer enhancement in melting of n-Octadecane under gravitational and electrohydrodynamics (EHD) forces, *J. Electrostat.* 92 (2018) 31–37.
- [36] D. Nakhla, J.S. Cotton, Effect of electrohydrodynamic (EHD) forces on charging of a vertical latent heat thermal storage module filled with octadecane, *Int. J. Heat Mass Transfer* 167 (2021) 120828.
- [37] G. McGranaghan, A. Robinson, The mechanisms of heat transfer during convective boiling under the influence of AC electric fields, *Int. J. Heat Mass Transfer* 73 (2014) 376–388.
- [38] Z. Sun, P. Yang, K. Luo, J. Wu, Experimental investigation on the melting characteristics of n-octadecane with electric field inside macrocapsule, *Int. J. Heat Mass Transfer* 173 (2021) 121238.
- [39] Z. Sun, K. Luo, J. Wu, Experimental study on the melting characteristics of n-octadecane with passively installing fin and actively applying electric field, *Int. Commun. Heat Mass Transfer* 127 (2021) 105570.
- [40] Z. Sun, Y. Zhang, K. Luo, A.T. Pérez, H. Yi, J. Wu, Experimental investigation on melting heat transfer of an organic material under electric field, *Exp. Therm. Fluid Sci.* 131 (2022) 110530.
- [41] Z. Sun, K. Luo, H. Yi, J. Wu, Experimental study on the melting heat transfer of octadecane with passively adding graphene and actively applying an electric field, *Int. J. Heat Mass Transfer* 204 (2023) 123845.
- [42] A. Hassan, J.S. Cotton, Investigation of the role of electrohydrodynamic forces on the heat transfer enhancement and solid extraction during melting of paraffin wax under constant temperature boundary conditions, *Int. J. Heat Mass Transfer* 204 (2023) 123831.
- [43] K. Luo, A.T. Pérez, J. Wu, H.-L. Yi, H.-P. Tan, Efficient Lattice Boltzmann method for electrohydrodynamic solid-liquid phase change, *Phys. Rev. E* 100 (1) (2019) 013306.
- [44] C.-L. Lu, X.-L. Gao, J. Wu, K. Luo, H.-L. Yi, Heat transfer enhancement analysis of electrohydrodynamic solid-liquid phase change via lattice Boltzmann method, *Appl. Therm. Eng.* 194 (2021) 117112.
- [45] R.D. Selvakumar, L. Qiang, L. Kang, P. Traoré, J. Wu, Numerical modeling of solid-liquid phase change under the influence an external electric field, *Int. J. Multiph. Flow* 136 (2021) 103550.
- [46] R.D. Selvakumar, S. Vengadesan, Combined effects of buoyancy and electric forces on non-isothermal melting of a dielectric phase change material, *Int. J. Multiph. Flow* 151 (2022) 104029.
- [47] H.E. Endigeri, R.D. Selvakumar, S. Vengadesan, Solid-liquid phase change subjected to unipolar charge injection from a circular wire electrode, *Int. J. Heat Mass Transfer* 194 (2022) 123120.
- [48] E.D. Fylladitakis, M.P. Theodoridis, A.X. Moronis, Review on the history, research, and applications of electrohydrodynamics, *IEEE Trans. Plasma Sci.* 42 (2) (2014) 358–375.

- [49] M. Kibria, M. Anisur, M. Mahfuz, R. Saidur, I. Metselaar, Numerical and experimental investigation of heat transfer in a shell and tube thermal energy storage system, *Int. Commun. Heat Mass Transfer* 53 (2014) 71–78.
- [50] S. Seddegh, X. Wang, A.D. Henderson, Numerical investigation of heat transfer mechanism in a vertical shell and tube latent heat energy storage system, *Appl. Therm. Eng.* 87 (2015) 698–706.
- [51] R. Senthil, B.M.S. Punniakodi, D. Balasubramanian, X.P. Nguyen, A.T. Hoang, V.N. Nguyen, Numerical investigation on melting and energy storage density enhancement of phase change material in a horizontal cylindrical container, *Int. J. Energy Res.* 46 (13) (2022) 19138–19158.
- [52] P. Atten, Electrohydrodynamic instability and motion induced by injected space charge in insulating liquids, *IEEE Trans. Dielectr. Electr. Insul.* 3 (1) (1996) 1–17.
- [53] J. Wu, P. Traoré, A finite-volume method for electro-thermoconvective phenomena in a plane layer of dielectric liquid, *Numer. Heat Transfer A* 68 (5) (2015) 471–500.
- [54] K. Luo, J. Wu, A.T. Pérez, H.-L. Yi, H.-P. Tan, Stability analysis of electroconvection with a solid-liquid interface via the Lattice Boltzmann method, *Phys. Rev. Fluids* 4 (8) (2019) 083702.
- [55] A. Brent, V.R. Voller, K. Reid, Enthalpy-porosity technique for modeling convection-diffusion phase change: application to the melting of a pure metal, *Numer. Heat Transfer A* 13 (3) (1988) 297–318.
- [56] M. Faden, A. König-Haagen, D. Brüggemann, An optimum enthalpy approach for melting and solidification with volume change, *Energies* 12 (5) (2019) 868.
- [57] M. Rathod, J. Banerjee, Experimental investigations on latent heat storage unit using paraffin wax as phase change material, *Exp. Heat Transfer* 27 (1) (2014) 40–55.
- [58] B. Favier, J. Purseed, L. Duchemin, Rayleigh–Bénard convection with a melting boundary, *J. Fluid Mech.* 858 (2019) 437–473.
- [59] R.D. Selvakumar, J. Wu, J. Huang, P. Traoré, Electro-thermo-convection in a differentially heated square cavity under arbitrary unipolar injection of ions, *Int. J. Heat Fluid Flow* 89 (2021) 108787.
- [60] N.I. Ibrahim, F.A. Al-Sulaiman, S. Rahman, B.S. Yilbas, A.Z. Sahin, Heat transfer enhancement of phase change materials for thermal energy storage applications: A critical review, *Renew. Sustain. Energy Rev.* 74 (2017) 26–50.